Noname manuscript No.
(will be inserted by the editor)

Pantographic metamaterials: an example of mathematically-driven design and of its technological challenges

Francesco dell'Isola · Pierre Seppecher · Jean Jacques Alibert · Tomasz Lekszycki · Roman Grygoruk · Marek Pawlikowski · David Steigmann · Ivan Giorgio · Ugo Andreaus · Emilio Turco · Maciej Gołaszewski · Nicola Rizzi · Claude Boutin · Victor Eremeyev · Anil Misra · Luca Placidi · Emilio Barchiesi · Leopoldo Greco · Massimo Cuomo · Antonio Cazzani · Alessandro Della Corte · Antonio Battista · Daria Scerrato · Inna Zurba Eremeeva · Yosra Rahali · Jean-François Ganghoffer · Wolfgang Müller · Gregor Ganzosch · Mario Spagnuolo · Aron Pfaff · Katarzyna Barcz · Klaus Hoschke · François Hild

Received: date / Accepted: date

Francesco dell'Isola
Dipartimento di Ingegneria Strutturale e Geotecnica, Università degli Studi di Roma "La Sapienza." Via Eudossiana 18, 00184 Roma, Italy.
International Research Center M&MoCS, Università degli Studi dell'Aquila. Via Giovanni Gronchi 18 - Zona industriale di Pile, 67100 L'Aquila, Italy.
Dipartimento di Ingegneria Civile, Edile-Architettura e Ambientale, Università degli Studi dell'Aquila. Via Giovanni Gronchi 18 - Zona industriale di Pile, 67100 L'Aquila, Italy.

Pierre Seppecher
Institut de Mathématiques de Toulon, Université de Toulon et du Var. Avenue de l' Université, BP 132, 83957 La Garde, Cedex, France.
International Research Center M&MoCS, Università degli Studi dell'Aquila. Via Giovanni Gronchi 18 - Zona industriale di Pile, 67100 L'Aquila, Italy.

Jean Jacques Alibert
Institut de Mathématiques de Toulon, Université de Toulon et du Var. Avenue de l' Université, BP 132, 83957 La Garde, Cedex, France.

Tomasz Lekszycki
International Research Center M&MoCS, Università degli Studi dell'Aquila. Via Giovanni Gronchi 18 - Zona industriale di Pile, 67100 L'Aquila, Poland.
Institute of Mechanics and Printing, Warsaw University of Technology. 85 Narbutta Street, 02-524 Warsaw, Poland.
Department of Experimental Physiology and Pathophysiology, Medical University of Warsaw. 1b Banacha Street, 02-097 Warsaw, Poland.

Roman Grygoruk
Institute of Mechanics and Printing, Warsaw University of Technology. 85 Narbutta Street, 02-524 Warsaw, Poland.

Marek Pawlikowski
Institute of Mechanics and Printing, Warsaw University of Technology. 85 Narbutta Street, 02-524 Warsaw, Poland.

David Steigmann
Department of Mechanical Engineering, University of California at Berkeley. 6133 Etcheverry Hall, Mailstop 1740, Berkeley, California.

Ivan Giorgio
International Research Center M&MoCS, Università degli Studi dell'Aquila. Via Giovanni Gronchi 18 - Zona industriale di Pile, 67100 L'Aquila, Italy.

Ugo Andreaus
Dipartimento di Ingegneria Strutturale e Geotecnica, Università degli Studi di Roma "La Sapienza." Via Eudossiana 18, 00184 Roma, Italy.

Emilio Turco
Dipartimento di Architettura, Design, Urbanistica, Università degli Studi di Sassari. Asilo Sella, Via Garibaldi 35 (I piano) 07041 Alghero (SS), Italy.
International Research Center M&MoCS, Università degli Studi dell'Aquila. Via Giovanni Gronchi 18 - Zona industriale di Pile, 67100 L' Aquila, Italy.

Maciej Gołaszewski
Institute of Mechanics and Printing, Warsaw University of Technology. 85 Narbutta Street, 02-524 Warsaw, Poland.

Nicola Rizzi
Dipartimento di Architettura, Università degli studi Roma Tre. Via della Madonna dei Monti 40, 00184 Roma, Italy.

Claude Boutin
Université de Lyon, Ecole Nationale des Travaux Publics de l'Etat, LGCB CNRS 5513 - CeLyA, 69518 Vaulx-en-Velin Cedex, France.

Victor Eremeyev
International Research Center M&MoCS, Università degli Studi dell'Aquila. Via Giovanni Gronchi 18 - Zona industriale di Pile, 67100 L'Aquila, Italy.
Mathematics, Mechanics and Computer Science Department, South Federal University. Milchakova, str., 8a, Rostov-on-Don, 344090, Russia.
Faculty of Mechanical Engineering and Aeronautics, Rzeszòw University of Technology. al. Powstańcòw Warszawy 8 35-959 Rzeszòw, Poland.

Anil Misra
International Research Center M&MoCS, Università degli Studi dell'Aquila. Via Giovanni Gronchi 18 - Zona industriale di Pile, 67100 L'Aquila, Italy.
Civil, Environmental and Architectural Engineering, Department The University of Kansas. 1530 W. 15th Street, Lawrence, KS 66045-7609, Kansas.

Luca Placidi
International Research Center M&MoCS, Università degli Studi dell'Aquila. Via Giovanni Gronchi 18 - Zona industriale di Pile, 67100 L'Aquila, Italy.
Engineering Faculty, International Telematic University Uninettuno. C.so Vittorio Emanuele II 39, 00186 Roma, Italy.

Emilio Barchiesi
Dipartimento di Ingegneria Strutturale e Geotecnica, Università degli Studi di Roma "La Sapienza." Via Eudossiana 18, 00184 Roma, Italy.
International Research Center M&MoCS, Università degli Studi dell'Aquila. Via Giovanni Gronchi 18 - Zona industriale di Pile, 67100 L'Aquila, Italy.

Leopoldo Greco
International Research Center M&MoCS, Università degli Studi dell'Aquila. Via Giovanni Gronchi 18 - Zona industriale di Pile, 67100 L'Aquila, Italy.
Dipartimento di Ingegneria Civile ed Ambientale (sezione di Ingegneria Strutturale), Università di Catania. Edificio Polifunzionale, IV piano. Viale Andrea Doria, 6 I - 95125 Catania, Italy.

Massimo Cuomo
International Research Center M&MoCS, Università degli Studi dell'Aquila. Via Giovanni Gronchi 18 - Zona industriale di Pile, 67100 L'Aquila, Italy.
Dipartimento di Ingegneria Civile ed Ambientale (sezione di Ingegneria Strutturale), Università di Catania. Edificio Polifunzionale, IV piano. Viale Andrea Doria, 6 I - 95125 Catania, Italy.

Antonio Cazzani
Dipartimento di Ingegneria Civile, Ambientale e Architettura, Università degli studi di Cagliari. Via Marengo 2, Cagliari, Italy.

Alessandro Della Corte
International Research Center M&MoCS, Università degli Studi dell'Aquila. Via Giovanni Gronchi 18 - Zona industriale di Pile, 67100 L'Aquila, Italy.
Dipartimento di Ingegneria Civile, Edile-Architettura e Ambientale, Università degli Studi dell'Aquila. Via Giovanni Gronchi 18 - Zona industriale di Pile, 67100 L'Aquila, Italy.

Antonio Battista
International Research Center M&MoCS, Università degli Studi dell'Aquila. Via Giovanni Gronchi 18 - Zona industriale di Pile, 67100 L'Aquila,Italy.
Laboratoire des Sciences de l'Ingénieur pour l' Environnement, Université de La Rochelle. 23 avenue Albert Einstein BP 33060, 17031 La Rochelle, Italy.
Dipartimento di Ingegneria e Scienze dell'Informazione e Matematica, Università degli Studi dell'Aquila. Via Vetoio, Coppito, 67100 L'Aquila, Italy.

Daria Scerrato
International Research Center M&MoCS, Università degli Studi dell'Aquila. Via Giovanni Gronchi 18 - Zona industriale di Pile, 67100 L'Aquila, Italy.

Inna Zurba Eremeeva
International Research Center M&MoCS, Università degli Studi dell'Aquila. Via Giovanni Gronchi 18 - Zona industriale di Pile, 67100 L'Aquila, Italy.

Yosra Rahali
Laboratoire d'Energétique et de Mécanique Théorique et Appliquée, University of Lorraine. 2 Avenue de la Foret de Haye BP 90161 54505 Vandoeuvre-lés-Nancy cedex, France.

Jean-François Ganghoffer
International Research Center M&MoCS, Università degli Studi dell'Aquila. Via Giovanni Gronchi 18 - Zona industriale di Pile, 67100 L'Aquila, Italy.
Laboratoire d'Energétique et de Mécanique Théorique et Appliquée, University of Lorraine. 2 Avenue de la Foret de Haye BP 90161 54505 Vandoeuvre-lés-Nancy cedex, France.

Wolfgang Müller
Faculty of Mechanics, Berlin University of Technology. Einsteinufer 5, 10587 Berlin, Germany.

Gregor Ganzosch
Faculty of Mechanics, Berlin University of Technology. Einsteinufer 5, 10587 Berlin, Germany.

Mario Spagnuolo
Laboratoire des Sciences des Procédés et des Matériaux, Université Paris 13. Campus de Villetaneuse 99 avenue Jean-baptiste Clément 93430 Villetaneuse, France.

Aron Pfaff
Fraunhofer Institute for High-Speed Dynamics, Ernst-Mach-Institut. Eckerstraße 4, 79104 Freiburg, Germany.

Katarzyna Barcz
Institute of Mechanics and Printing, Warsaw University of Technology. 85 Narbutta Street, 02-524 Warsaw, Poland.

Klaus Hoschke
Fraunhofer Institute for High-Speed Dynamics, Ernst-Mach-Institut. Eckerstraße 4, 79104 Freiburg, Germany.

François Hild
Laboratoire de Mécanique et Technologie (LMT), ENS Paris-Saclay / CNRS / Université Paris-Saclay, 61 avenue du Président Wilson, 94235 Cachan Cedex, France.

Abstract In this paper we account for the research efforts that have been started, for some among us, already since 2003, and aimed to the design of a class of exotic architectured, optimized (meta) materials. At the first stage of these efforts, as it often happens, the research was based on the results of mathematical investigations. The problem to be solved was stated as follows: determine the material (micro)structure governed by those equations that specify a desired behavior. Addressing this problem has led to the synthesis of second gradient materials. In the second stage, it has been necessary to develop numerical integration schemes and the corresponding codes for solving, in physically relevant cases, the chosen equations. Finally, it has been necessary to physically construct the theoretically synthesized microstructures. This has been possible by means of the recent developments in rapid prototyping technologies, which allow for the fabrication of some complex (micro)structures considered, up to now, to be simply some mathematical dreams. We show here a panorama of the results of our efforts i) in designing pantographic meta-materials, ii) in exploiting the modern technology of rapid prototyping, and iii) in the mechanical testing of many real prototypes. Among the key findings that have been obtained there are the following ones: pantographic meta-materials i) undergo very large deformations while remaining in the elastic regime, ii) are very tough in resisting to damage phenomena, iii) exhibit robust macroscopic mechanical behavior with respect to minor changes in their microstructure and micromechanical properties, iv) have superior strength to weight ratio, v) have predictable damage behavior, and vi) possess physical properties that are critically dictated by their geometry at the microlevel.

Introduction

Like every other human activity, the design, manufacturing and testing of prototypes of novel materials having a complex and purpose-tailored (micro)structure need the organized efforts of many specialists having a large scope of competence. Therefore, the present work needed the collaboration of many scientists, each one with his/her own specific competence. The order of the authors of this paper has been formed with a simple criterion: it is related to the length of the time period that has seen their involvement in the described joint research efforts and, therefore, does not express any evaluation of the importance of each contribution.

Let us note that, in this paper, no specific length scale is attached to the word "micro." Specifically, with its use it is meant that at one or at multiple smaller (with respect to the unique macroscale corresponding to that at which phenomena are observed) length scales the material is made of complex microstructures: they consist in the organization of the distribution of matter and its (possibly varying) physical properties.

The aim of this paper is to account, in a unique panoramic view, for the research efforts that we have started (at least the first ones among us) since 2003 and that has produced, in our opinion, some interesting results. The aim of the investigations was more specifically i) to design novel and exotic architectured metamaterials based on a mathematical understanding of the related mechanical problems and on suitably designed numerical simulations, ii) to build the designed prototypes by using 3D printing technology, iii) to test with sensitive apparatuses the so-built prototypes, iv) to elaborate the obtained data with modern image correlation techniques v) to produce a careful model fitting of the experimental data by means of the systematic use of numerical simulations and vi) to compare the proposed models with experimental evidence.

At the first stage of the research effort, as it often happens, the problem was approached from a theoretical point of view. The mathematical models, which were initially introduced, belong to the class of generalized continua: the introduced independent kinematic fields include not only the displacement field but, eventually, also microstretch and/or microrotation fields. The particular class of second gradient continua was more specifically considered: in these media, the strain energy depends on the displacement gradient and on its second gradient. The reasons of their name is therefore clear: in second gradient continua the strain energy may depend on the second gradient of displacement. Second gradient continua can be regarded as media endowed with a tensorial microstructure in which a constraint is applied: it requires that the microstructure tensor be equal

to the placement gradient. The problem to be solved was: given a desired behavior, to find at first the evolution equations modeling such a behavior and then to characterize the material (micro)structure governed by the chosen equations.

In the second stage it was necessary to develop numerical integration schemes and the corresponding codes for solving, in physically relevant cases, the equations chosen to describe the desired behavior. Finally, it was necessary to build the microstructures. This was possible by means of the recent developments of rapid prototyping technologies, which allows for the fabrication of those which, up to now, were simply mathematical dreams.

In this paper we show the results of our efforts in designing pantographic metamaterials, in the mechanical testing of real prototypes, and evidence is provided on their exotic behavior. With the latest advancements (e.g. 3D-printing technology and, more generally, of rapid prototyping techniques), the small scale production of materials with complex geometries has become more affordable than ever [1–4]. The exploitation of these new technologies has made possible the development in the last few years of materials with very different sub-structures.

One of the research goals whose achievement has been sped-up by rapid prototyping is to determine and study new microstructures that, at a well-specified macroscopic scale, exhibit a behavior that can be described by non-standard mathematical models like generalized continuum theories. Many of these theories, that today are being called "generalized" (as opposed to "classical" theories), were formulated before or together with so-called "classical" theories and then lost [5, 6]. It is possible to state that some of these theories were already known at least two centuries ago [7,8]. Pantographic structures (Fig. 1) have been proposed as a meta-material [9], which is well described by second gradient continuum theories [10–12].

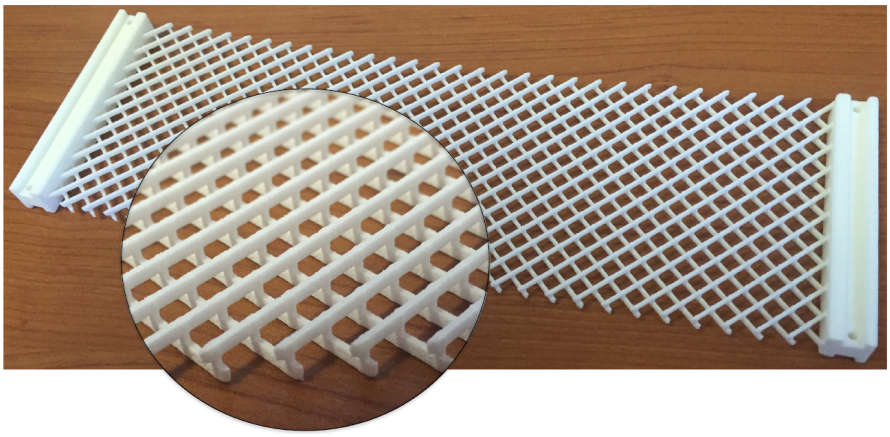

Fig. 1 Example of pantographic structure [13]

1 Modelling and experiments in elastic regime

The theoretical interest in pantographic structures derives from the fact that, in order to describe their exotic phenomenology, one has to utilize higher gradient continuum theories [14,15] or micromophic theories [16,17] with the related problem of homogenization [18] and of different strategies for numerical integration [19,20].

1.1 Homogenization of periodic truss modular structures

Throughout the history of Mechanics, several multiscale procedures have been developed in order to relate macromodels with micromodels, the first attempts tracing back to Maxwell and de Saint-Venant [21]. An approach that has proven to be effective is based on the postulate of a macroscopic and a microscopic model and of a kinematic correspondence between the deformations defined within the two models. Successively, it is postulated that the power expended in corresponding motions coincides. In this way it is possible to obtain the coefficients of the constitutive equations of the macromodel in terms of properties of the building blocks constituting the microscopic model. Thus, in this case, the macromodel is not the result of the homogenization process but is, instead, assumed a priori. Formal asymptotic expansion can help to encompass this difficulty and a microscopic model made up of linear Euler beams leads to a simple macroscopic second gradient model of a 1D planar beam [11]. The structure that is considered at the microlevel is the so-called pantographic structure (Fig. 2). It is assumed that the considered pantographic microstructure is made up of a very large number of small modules and the limit behavior when such a number tends to infinity, i.e. the homogenized macromodel, is studied. Using the technique of Gamma-convergence, it is proven that the homogenized model is the postulated second gradient model [11]. Successively, a modified (Warren-type) pantographic structure is proposed as micro-model in order to get for the first time a third gradient planar beam model (Fig. 3), whose general properties were already studied by Mindlin and Tiersten [22], and Dillon and Perzyna [23]. Such structures possess other floppy modes (i.e. placements for which the strain energy vanishes) than, trivially, rigid motions. The pantographic beam does not store any energy when undergoing uniform extension, while the Warren-type pantographic beam does not store any energy when undergoing uniform flexure.

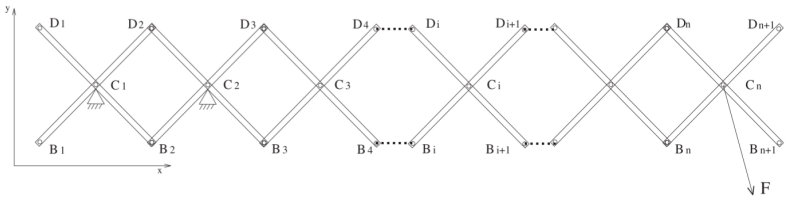

Fig. 2 Pantographic microstructure considered in Ref. [11].

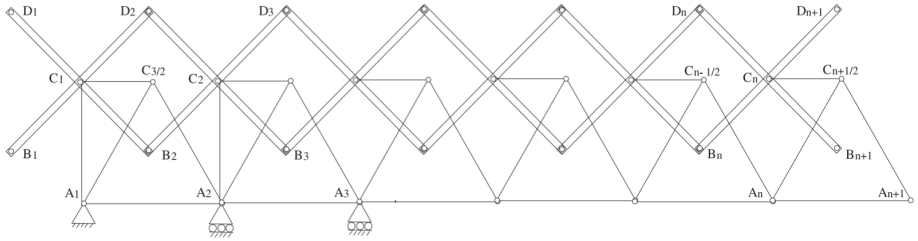

Fig. 3 Warren-type pantographic microstructure [11].

In Ref. [24], formal asymptotic expansion procedures, already employed [13,11], are systematically considered in the framework of linear elasticity in order to determine the effective behavior of periodic structures made of welded elastic bars. Noting that flexural and torsional stiffnesses of isotropic homogeneous elastic bars are much smaller than the extensional one entails an asymptotic

rescaling of stiffnesses giving rise to interesting macromodels. In Ref. [24] different examples of two dimensional or three dimensional microstructures that lead to generalized 1D, 2D or 3D continua like Timoshenko beam, Mindlin-Reissner plate, strain gradient, Cosserat, or micromorphic continua are provided.

Reference [25], in the spirit of pantographic fabrics, addresses one of the main challenges in the modern theory of materials: the determination of those microstructures that produce, at the macrolevel, a class of metamaterials whose elastic range is many orders of magnitude wider than the one exhibited by "conventional" materials. With pantographic microstructures, which are made of "long" microbeams, it is possible to obtain metamaterials whose elastic range spans up to an elongation exceeding 30%. It is shown that the same behavior can be obtained by means of an internal microstructure based on a king post pattern (Fig. 4). This solution shows many advantages, namely, it only involves microbeams; all beams are only undergoing extension or contraction; all internal constraints are terminal pivots. While the elastic strain energy can be determined as easily as in the case of a long-beam microstructure, the proposed design seems to have remarkable advantages: it seems to be more damage resistant and, therefore, to be able to have a wider elastic range; it can be obtained with the same three-dimensional printing technology; it seems to be less subject to compression buckling. The following analyses were carried out: (i) the derivation of Hencky-type discrete models for king post trusses, (ii) the application of an effective integration scheme to a class of relevant deformation tests for the proposed metamaterial and (iii) the numerical determination of an equivalent second gradient continuum model.

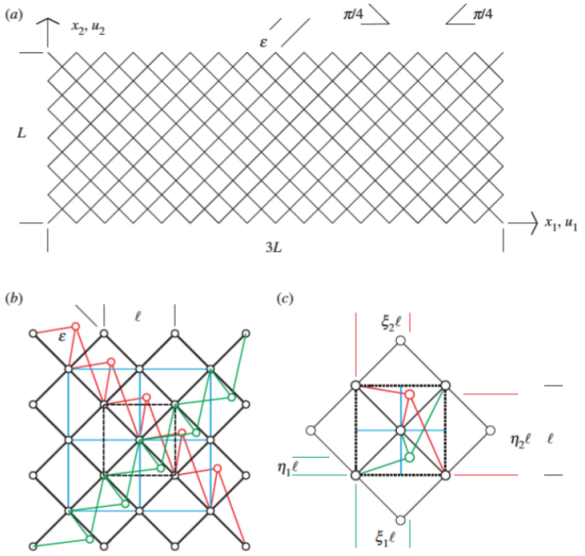

Fig. 4 King post pantographic lattice: geometry (a), pantographic rods (in black), king post rods (in red and green), auxiliary rods (in cyan) (b) and king post geometric parameters (c).

1.2 Pipkin elastic plate model with inextensible fibers

Starting from a number of papers by Pipkin et al. [26–33], 2D continua consisting of two orthogonal families of inextensible fibers were considered [34] and an adaptation to the case of pantographic structures has been presented [10,35]. First, a $2D$ continuum, whose reference shape is given by the rectangular domain $\Omega \subset \mathbb{R}^2$ with the tallest side three times longer than the shorter one, has been considered. Considering only planar motions, the current shape of Ω is described by the suitably

regular macro-placement $\boldsymbol{\chi}:\ \Omega \to \mathbb{R}^2$, with $(X_1, X_2) \overset{\boldsymbol{\chi}}{\mapsto} (x_1, x_2)$. An orthogonal frame of reference $(\mathcal{O}, \xi_1, \xi_2)$, whose orientation is the same of the inextensible fibers in the reference configuration and whose coordinates are dimensionless, is introduced. Accordingly, we have

$$\xi_1 := \frac{1}{l}(X_1 - X_2) + \frac{1}{2}\ ,\ \ \xi_2 := \frac{1}{l}(X_1 + X_2) + \frac{1}{2}. \tag{1}$$

A graphical depiction of the introduced quantities is given in Fig. 5. A pair (D_1, D_2) of orthonormal vectors, the basis associated with the frame of reference $(\mathcal{O}, \xi_1, \xi_2)$, is further introduced. The two vectors D_1 and D_2 are tangent to the two families of fibers in the reference configuration. The inextensibility constraint can be encoded in the following way: a curve β is inextensible for a placement $\boldsymbol{\chi}$ if, for every part α of β, $\boldsymbol{\chi}(\alpha)$ has the same length of α.

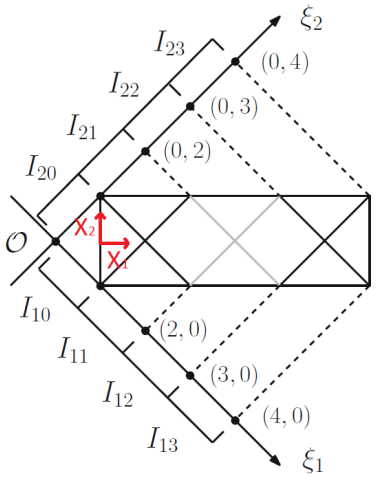

Fig. 5 Material (Lagrangian) coordinates adapted to inextensible fiber configuration [10].

By definition d_1 and d_2 are considered to be the push-forward vectors, in the current configuration, of the vectors D_1 and D_2, respectively, i.e. $d_\alpha = FD_\alpha,\ \alpha = 1, 2$, where $F = \nabla\boldsymbol{\chi}$. The inextensibility constraint implies that $\|d_1(\xi_1, \xi_2)\| = \|d_2(\xi_1, \xi_2)\| = 1$ for all (ξ_1, ξ_2) such that $\boldsymbol{\chi}$ is locally continuously differentiable. In the celebrated Rivlin paper [36], it is stated that when $\boldsymbol{\chi}$ is twice continuously differentiable on an open simply linearly connected subset Δ of Ω, the fiber inextensibility assumption allows the following representation formula

$$\boldsymbol{\chi}^{\Delta}(\xi_1, \xi_2) = \boldsymbol{\chi}_1^{\Delta}(\xi_1) + \boldsymbol{\chi}_2^{\Delta}(\xi_2) \tag{2}$$

to be found for the restriction to Δ of the placement. If $\mu_1^{\Delta}(\xi_1)$ and $\nu_1^{\Delta}(\xi_1)$ denote the projections of $\boldsymbol{\chi}_1^{\Delta}(\xi_1)$ on D_1 and D_2, respectively, and $\nu_2^{\Delta}(\xi_2)$ and $\mu_2^{\Delta}(\xi_2)$ the projections of $\boldsymbol{\chi}_2^{\Delta}(\xi_1)$ on D_1 and D_2, respectively, then

$$\boldsymbol{\chi}_1^{\Delta}(\xi_1) = \mu_1^{\Delta}(\xi_1)D_1 + \nu_1^{\Delta}(\xi_1)D_2 \text{ and } \boldsymbol{\chi}_2^{\Delta}(\xi_2) = \nu_2^{\Delta}(\xi_2)D_1 + \mu_2^{\Delta}(\xi_2)D_2 \tag{3}$$

The map $\boldsymbol{\chi}$ is assumed to be piece-wise twice continuously differentiable. It is worth noting that the matrix representation of F on the subset Δ and for the frame of reference defined by D_1 and D_2 is

$$[F^{\Delta}]_{(D_1,D_2)} = \begin{bmatrix} \mu_{1,1}^{\Delta}(\xi_1) & \nu_{2,2}^{\Delta}(\xi_2) \\ \nu_{1,1}^{\Delta}(\xi_1) & \mu_{2,2}^{\Delta}(\xi_2) \end{bmatrix} \tag{4}$$

and that the functions $\boldsymbol{\chi}_\alpha^{\Delta}(\xi_\alpha)$ $(\alpha = 1,2)$ are determined up to two scalar constants C_1 and C_2, i.e. if the decomposition (2) holds with the representation (3), then the following alternative representation holds

$$\begin{aligned}\boldsymbol{\chi}_1^{\Delta}(\xi_1) &= \left(\mu_1^{\Delta}(\xi_1) + C_1\right) D_1 + \left(\nu_1^{\Delta}(\xi_1) + C_2\right) D_2 \\ \boldsymbol{\chi}_2^{\Delta}(\xi_2) &= \left(\nu_2^{\Delta}(\xi_2) - C_1\right) D_1 + \left(\mu_2^{\Delta}(\xi_2) - C_2\right) D_2\end{aligned} \tag{5}$$

The inextensibility constraint, together with the assumption that the map χ be piecewise C^2, implies that there exist two quantities $\vartheta_1^{\Delta}(\xi_1)$ and $\vartheta_2^{\Delta}(\xi_2)$ such that

$$d_1^{\Delta} = \cos\vartheta_1(\xi_1)D_1 + \sin\vartheta_1(\xi_1)D_2 \quad \text{and} \quad d_2^{\Delta} = \sin\vartheta_2(\xi_2)D_1 + \cos\vartheta_2(\xi_2)D_2 \tag{6}$$

The above statement stands since d_1^{Δ} and d_2^{Δ} belong to $S_2 = \{x \in \mathbb{R}^2 : \ \|x\| = 1\}$.

Let Σ_1 and Σ_2 denote the left and right short sides, respectively, of the boundary $\partial\Omega$ of Ω. The following boundary conditions are considered:

1. vanishing displacement on Σ_1;
2. non-vanishing displacement u_0 on Σ_2.

Because of fiber inextensibility, the boundary conditions on Σ_1 and Σ_2 determine the placement field not just at the boundary, but also in some regions of the interior of Ω [34] , i.e. on the regions Δ_{00} and Δ_{33} of Fig. 6.

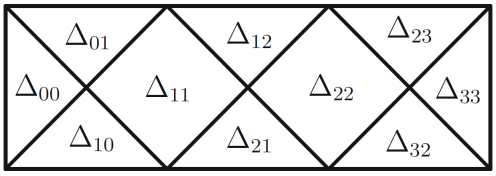

Fig. 6 Domain pattern induced by the boundary conditions [10].

Hence, the space of admissible placements for the Pipkin continuum under study is uniquely determined by the continuous piecewise twice continuously differentiable fields $\mu_1(\xi_1)$ and $\mu_2(\xi_2)$. In particular, given the boundary conditions i.e. $\mu(\xi)$ is known on Δ_{00} and Δ_{33} (for $\xi_\alpha \in [0,1]\cup[3,4]$), we are interested in determining $\mu_\alpha(\xi_\alpha)$ only for $\xi_\alpha \in [1,3]$. By looking at the ordinary differential equations

$$\frac{\mathrm{d}\mu_\alpha(\xi_\alpha)}{\mathrm{d}\xi_\alpha} = \cos\vartheta_\alpha(\xi), \ \alpha = 1,2 \tag{7}$$

which derive from Equation (13) and (6). Providing an integration constant through the continuity condition $\mu_\alpha(1) = 1$ at point $(1,1)$ uniquely defines the space of admissible placements for the Pipkin continuum by means of the fields $\vartheta_1(\xi_1)$ and $\vartheta_2(\xi_2)$.

In fiber-inextensible 2D Pipkin continua it is customary to introduce the *shear deformation* γ as a strain measure. The shear deformation is defined as the scalar product of the fiber directions in the deformed configuration and, reminding the inextensibility assumption and Equation (6), reads

$$\gamma(\xi_1,\xi_2) \coloneqq d_1 \cdot d_2 = \cos\left(\frac{\pi}{2} - \vartheta_1(\xi_1) - \vartheta_2(\xi_2)\right) = \sin\left(\vartheta_1(\xi_1) + \vartheta_2(\xi_2)\right) \tag{8}$$

The following kinematic constraint should be enforced

$$-\frac{\pi}{2} < \vartheta_1 + \vartheta_2 < \frac{\pi}{2} \ \ (\implies -1 < \gamma < 1) \tag{9}$$

if the case $\vartheta_1 + \vartheta_2 = \pm\frac{\pi}{2}$, which stands for overlapping fibers is to be avoided. Now that the space of fields $\vartheta_1(\xi_1)$ and $\vartheta_2(\xi_2)$ uniquely describe admissible placements, the strain energy density $W(\vartheta_1, \vartheta_2, \frac{\mathrm{d}\vartheta_1}{\xi_1}, \frac{\mathrm{d}\vartheta_2}{\xi_2})$ is introduced. It is assumed to have the form

$$W(\vartheta_1, \vartheta_2, \frac{\mathrm{d}\vartheta_1}{\xi_1}, \frac{\mathrm{d}\vartheta_2}{\xi_2}) = \alpha g(f(\gamma)) + \beta g(\|\nabla f(\gamma)\|) \tag{10}$$

with $g(x) = \frac{1}{2}x^2$. Different functions f have been studied [10,35], among which:

S $f(\gamma) = \gamma$
Q $f(\gamma) = \arcsin\gamma$
T $f(\gamma) = \tan(\arcsin\gamma)$

Henceforth the case $\alpha = 1$, $\beta = 0$ is referred to as *first gradient* (1g), and $\alpha = 0$, $\beta = 1$ as *second gradient* (2g). Numerical results show that final configurations obtained by using second gradient energies are smoother than those with the first gradient approach. In the following, numerical results will be reported for standard bias extension, shear and rotation tests, which confirm such a statement. Among all experiment, the bias test has been extensively analyzed. In a standard bias extension test, $u_{01} = u_{02} \coloneqq u_0$. Then a new property has to be enforced on the placement function $\boldsymbol{\chi}$, which holds true for the bias extension test, while not, e.g., for the shear tests that will be considered later on. Only placements functions that are symmetric with respect to the X_1 axis can be considered. With regard to the reference frame $(\mathcal{O}, \xi_1, \xi_2)$, this means that given a point P of coordinates (ξ, η) and its symmetric (with respect to X_1) P_S whose coordinates are (η, ξ), the conditions

$$d_1(P) \cdot D_\alpha = d_2(P_S) \cdot D_{3-\alpha} \ \alpha = 1, 2 \tag{11}$$

must be satisfied. They imply that $\nu_{1,1}(\xi) = \nu_{2,2}(\xi)$ and $\mu_{1,1}(\xi) = \mu_{2,2}(\xi)$ and in turn, given the boundary conditions, $\nu_1(\xi) = \nu_2(\xi) \coloneqq \nu(\xi)$ and $\mu_1(\xi) = \mu_2(\xi) \coloneqq \mu(\xi)$. It is thus possible to state that in a standard bias test the space of admissible placements for the Pipkin continuum is uniquely determined by the continuous piecewise twice continuously differentiable field $\mu(\xi)$. Since $\mu(\xi)$ is known on Δ_{00} and Δ_{33}, i.e. for $\xi \in [0,1] \cup [3,4]$, we are interested in determining $\mu(\xi)$ only for $\xi \in [1,3]$. By analyzing ordinary differential equations

$$\frac{\mathrm{d}\mu_\alpha(\xi)}{\mathrm{d}\xi} = \cos\vartheta_\alpha(\xi), \ \alpha = 1, 2 \tag{12}$$

it is concluded that $\vartheta_1(\xi) = \vartheta_2(\xi) \coloneqq \vartheta(\xi)$ with $\vartheta(\xi)$ a (possibly discontinuous) piecewise continuously differentiable field. Numerical results are shown in Figs. 7 and 8. Figure 7 provides a general overview of the qualitative differences among different choices of α, β and of the function f in Equation (10). In Fig. 8, a comparison between final shapes of the rectangular sample is reported when modelled with $1gT$ and $2gT$ strain energy densities. It is possible to notice that final shapes are much smoother when a second gradient model is employed, as strong variations of the field variable are penalized in the energy.

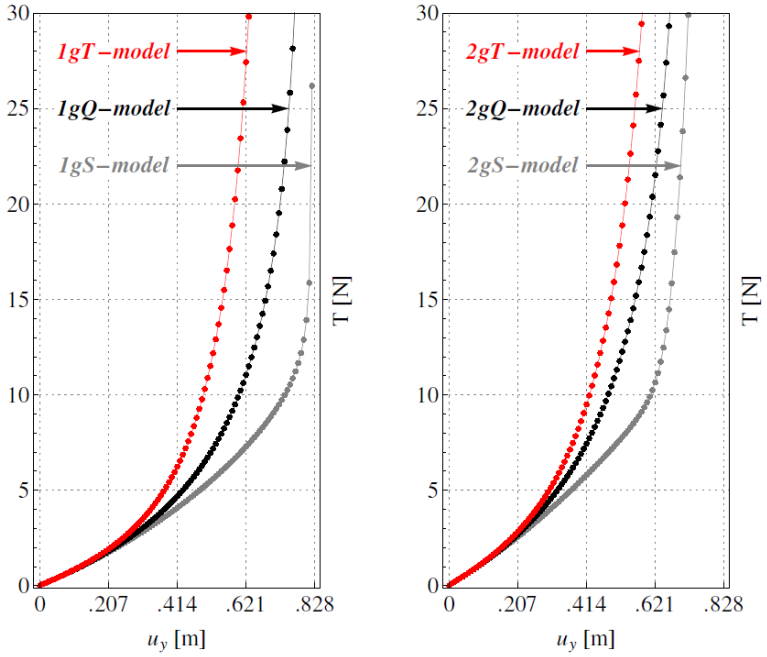

Fig. 7 Bias extension test. Resultant (normal) forces on the short side (computed by means of Castigliano's first theorem) versus vertical component of prescribed displacement: (a) first gradient energy models, (b) second gradient energy models.

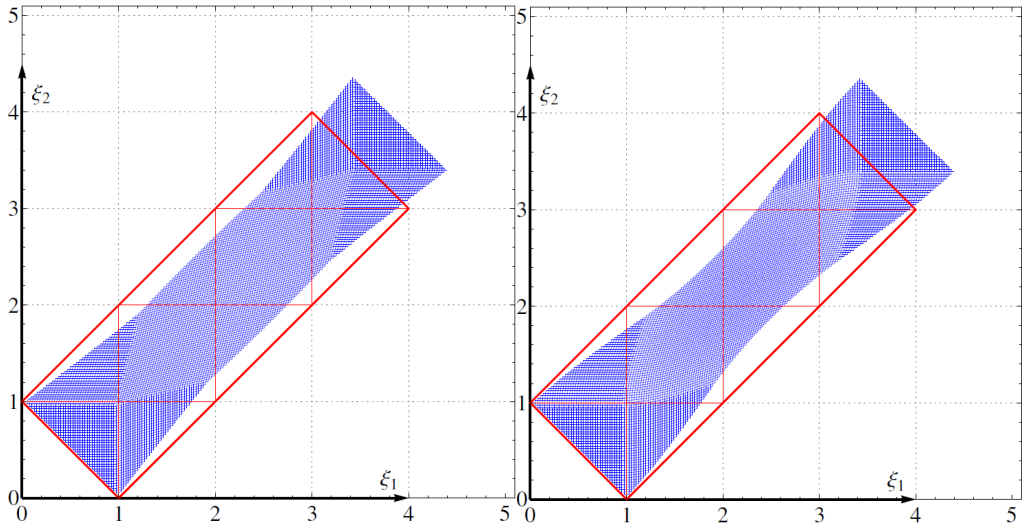

Fig. 8 Bias extension test. Reference and deformed configurations for the first gradient 1gT (left) and second gradient 2gT (right) models.

Let us now turn to reporting shear tests. Thus, the symmetry assumptions, which were previously introduced when dealing with the standard bias extension test, are no longer considered.

When modelling the shear test, the condition $u_{01} = -u_{02}$ holds. The results are shown in Figs. 9 and 10. In particular, Fig. 9 gives an overview of the qualitative differences among different choices of α, β and of the function f defined in Equation (10). The non-monotonicity of the $1gS$ and $2gS$ models is not physically grounded. Besides, in Fig. 10 comparisons between final shapes of the rectangular samples, modelled with $1gT$ and $2gT$ strain energy density, are reported. Again, it is possible to notice that final shapes are much smoother when a second gradient model is employed.

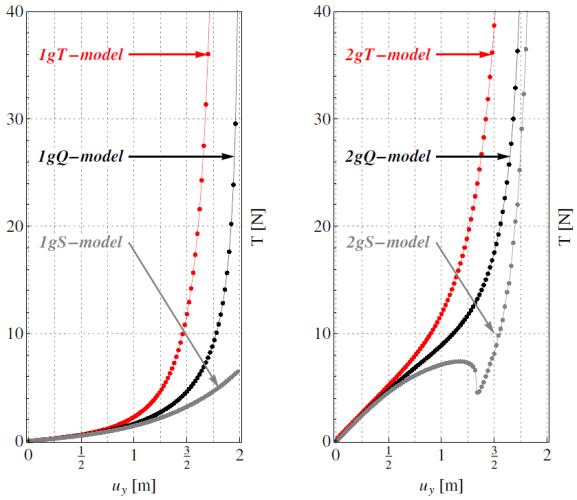

Fig. 9 Shear test. Resultant (shear) forces on the short side (computed by means of Castigliano's first theorem) versus vertical component of prescribed displacement: (a) first gradient energy models, (b) second gradient energy models.

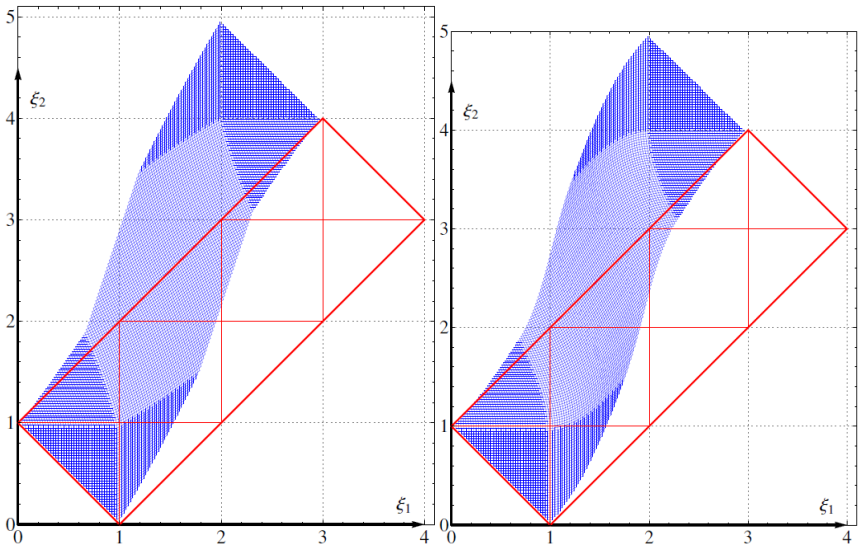

Fig. 10 Shear test. Reference and deformed configurations for the first gradient 1gT (left) and second gradient 2gT (right) models.

1.3 Discrete Hencky-type elastic plate model

A discrete approach has been introduced for pantographic structures [13], and subsequently studied [37,38]. Modelling assumptions for the micromodel are based on physically grounded considerations about the real microstructure of pantographic sheets and apply to the case of large deformations. In particular, trying to comply with reported experimental evidences [13,10], the extension of fibers is accounted for by connecting adjacent material particles with extensional springs. Moreover, at each node of the lattice, rotational springs, which are deformed when the angle spanned by two contiguous extensional springs is changed, are introduced. To account for the fact that such materials show two privileged material directions, a Lagrangian Cartesian orthonormal coordinate system is introduced. Its associated basis of unit vectors is (D_1, D_2) made of two orthonormal vectors that represent the directions of the families of fibers constituting the pantographic structure in the reference configuration. In such configuration the lattice body points are located at the positions

$$P_{i,j} = (i\epsilon, j\epsilon), \quad i = 0, 1, ..., N \text{ and } j = 0, 1, ..., M \tag{13}$$

and $p_{i,j}$ denotes the current configuration position of the body point placed at $P_{i,j}$ in the reference configuration. The body points at the nodes $P_{i,j}$ are connected by extensional springs along each one of the coordinate lines (Fig. 11) and their deformation energies depend on the distances between adjacent contiguous points in the current configuration, i.e. on the distance between $p_{i,j}$ and $p_{i,j+1}$ for the fibers parallel to D_1 in the reference configuration, and on the distance between $p_{i,j}$ and $p_{i+1,j}$ for the fibers parallel to D_2 in the reference configuration. The first type of extensional spring is characterized by the rigidity $k^1_{i,j}$ and the second kind by $k^2_{i,j}$. Such extensional rigidities are related to the extensional behavior, respectively, of the two families of fibers. As mentioned before, at each node there are also three rotational springs whose deformation energies depend respectively on the angles:

1. $\vartheta^1_{i,j}$ formed by the vectors $p_{i-1,j} - p_{i,j}$ and $p_{i+1,j} - p_{i,j}$,
2. $\vartheta^2_{i,j}$ formed by the vectors $p_{i,j-1} - p_{i,j}$ and $p_{i,j+1} - p_{i,j}$,
3. $\vartheta^3_{i,j}$ formed by the vectors $p_{i,j+1} - p_{i,j}$ and $p_{i+1,j} - p_{i,j}$.

The postulated strain energy for the microscopic Lagrangian discrete system having its configuration specified by the set of parameters $\{p_{i,j}\}$ reads

$$\begin{aligned} U(\{p_{i,j}\}) = &\sum_j \sum_i \frac{k^1_{i,j}}{2}(\|p_{i+1,j} - p_{i,j}\| - \epsilon)^2 + \sum_j \sum_i b^1_{i,j}(\cos\vartheta^1_{i,j} + 1) + \\ &+ \sum_j \sum_i \frac{k^2_{i,j}}{2}(\|p_{i,j+1} - p_{i,j}\| - \epsilon)^2 + \sum_j \sum_i b^2_{i,j}(\cos\vartheta^2_{i,j} + 1) + \\ &+ \sum_j \sum_i \frac{b^3_{i,j}}{2}\left|\vartheta^3_{i,j} - \frac{\pi}{2}\right|^\xi \end{aligned} \tag{14}$$

On the one hand, the rigidities $b^1_{i,j}$ and $b^2_{i,j}$ are related, respectively, to the bending behavior of the two families of fibers. The rigidities $b^3_{i,j}$, on the other hand, are associated with the torsional stiffness of the pivots connecting the two families of fibers, ξ being a parameter that is equal to 2 for a standard linear case.

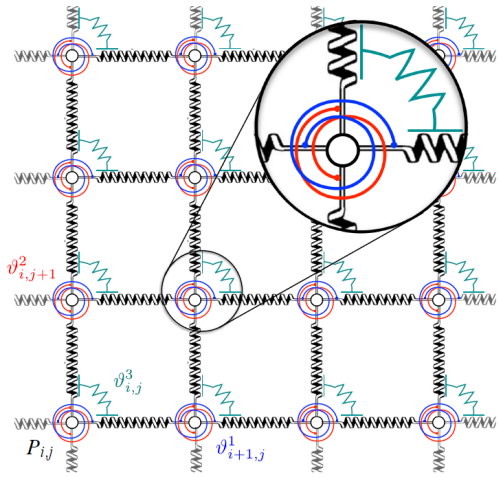

Fig. 11 Micromodel of a pantographic sheet with a detail of the three rotational springs [13]

In subsequent papers [37,38], the discrete (elastic) quasi-static Hencky-type spring model, made of extensional and rotational (i.e. torsional) springs is solved at each iteration by energy minimization. Even if the model does not contemplate external forces, it would be very easy to consider the discrete analogous forces leading, after a homogenization like the one presented later on, to external bulk forces and double forces. In Fig. 12 the equilibrium shape resulting from a standard bias extension test simulation using the strain energy (16) is shown, along with colors indicating the magnitude of internal forces on extensional springs computed in the current configuration, and whose expression is given in Ref. [38]. In the same manner, in Fig. 13, the equilibrium shape resulting from a shear test simulation is shown.

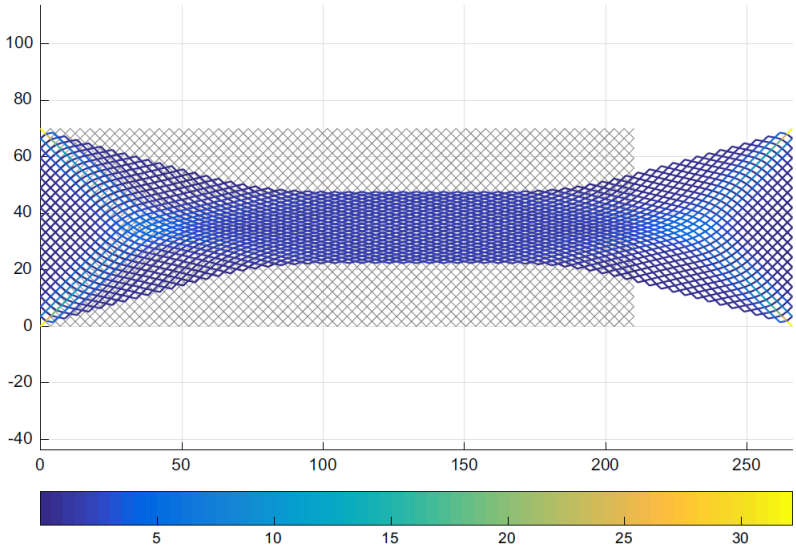

Fig. 12 Bias extension test simulation using the micromodel when $M = 20$ and $N = 60$: reference configuration (*gray*), current shape and *color bar* of the internal forces on extensional springs [38].

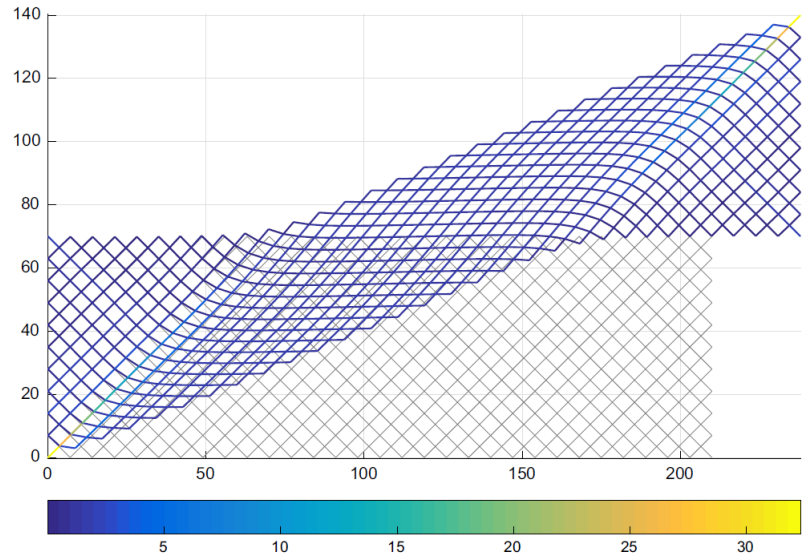

Fig. 13 Shear-extension test simulation using the micromodel: reference configuration (*gray*), current shape and *color bar* of the internal forces on extensional springs for $M = 10$ and $N = 30$ [38].

1.4 À la Piola homogenized elastic plate model

Considering the discrete Hencky-type micromodel presented above, a $2D$ continuum macromodel has been derived by means of micro-macro transitions. Expanding in truncated Taylor series the kinematic map [13] the micro-placement field of material particles at the nodes of the referential lattice is computed by means of the values, in such nodes, of a regular macro-placement and its first gradient. Such a map determines a unique micro-motion once a macro-motion is given. The micro-macro transition is obtained by equating the micro-strain energy with the macroscopic counterpart, thus obtaining a macroscopic Lagrangian surface density of strain energy in terms of the constitutive coefficients appearing in the postulated expression of the micro-strain energy. Numerical simulations with both discrete and homogenized models show that the homogenized model is representative of the microscopic response [37,38]. Following the notation introduced above, we now consider a $2D$ continuum whose reference shape is given by a rectangular domain $\Omega = [0, N\epsilon] \times [0, M\epsilon] \subset \mathbb{R}^2$. Very often, it is assumed that $N = 3M$, which is the standard relation between the width and height of a fabric specimen for experimental and numerical tests. By assuming planar motions, the current shape of Ω is described by regular macro-placement $\boldsymbol{\chi} : \Omega \to \mathbb{R}^2$. The kinematic map providing the micro-macro identification is the so-called Piola ansatz and we accordingly choose $p_{i,j} = \boldsymbol{\chi}(P_{i,j}) \quad \forall i = 1, ..., N, \ \forall j = 1, ..., M$. Assuming that $\boldsymbol{\chi}(\cdot)$ is at least twice differentiable at $P_{i,j}$, the following 2^{nd}-order approximations are obtained

$$\begin{aligned} \|p_{i+1,j} - p_{i,j}\| &= \|\boldsymbol{\chi}(P_{i+1,j}) - \boldsymbol{\chi}(P_{i,j})\| \backsimeq \epsilon \|F(P_{i,j})D_1 + \frac{\epsilon}{2}\nabla F(P_{i,j})|D_1 \otimes D_1\| \\ \|p_{i,j+1} - p_{i,j}\| &= \|\boldsymbol{\chi}(P_{i,j+1}) - \boldsymbol{\chi}(P_{i,j})\| \backsimeq \epsilon \|F(P_{i,j})D_2 + \frac{\epsilon}{2}\nabla F(P_{i,j})|D_2 \otimes D_2\| \end{aligned} \tag{15}$$

where F is the deformation gradient $\boldsymbol{\nabla\chi}$. The reader is referred to the original papers [37,38, 13] for further details. Equations (15) have been used for the homogenization procedure of two addends of Equation (14). In order to address the other three terms, the cosines of the angles $\vartheta^{\alpha}_{i,j}$ ($\alpha = 1, 2$) and $\vartheta^{3}_{i,j}$ are derived as functions of the macro-placement $\boldsymbol{\chi}$. Using analogous Taylor

expansions as those in Equation (15) neglecting $o(\epsilon^2)$ terms, and writing all quantities in terms of the displacement $\boldsymbol{\chi}$, the strain energy of the micromodel becomes

$$\begin{aligned} U(\{p_{i,j}\}) = &\sum_j \sum_i \sum_\alpha \frac{k^\alpha_{i,j}}{2}\epsilon^2(\|F(P_{i,j})D_\alpha + \frac{\epsilon}{2}\nabla F(P_{i,j})|D_\alpha \otimes D_\alpha\| - 1)^2 \\ &+ \sum_j \sum_i \sum_\alpha b^\alpha_{i,j}\left[\frac{\|\nabla F(P_{i,j})|D_\alpha \otimes D_\alpha\|^2}{\|F_{i,j}D_\alpha\|^2} - \left(\frac{F(P_{i,j})D_\alpha \cdot \nabla F(P_{i,j})|D_\alpha \otimes D_\alpha}{\|F_{i,j}D_\alpha\|^2}\right)^2\right]\frac{\epsilon^2}{2} \\ &+ \sum_j \sum_i \frac{b^3_{i,j}}{2}\left|\arccos\left(\frac{F(P_{i,j})D_1 \cdot F(P_{i,j})D_2}{\|F(P_{i,j})D_1\| \cdot \|F(P_{i,j})D_2\|}\right) - \frac{\pi}{2}\right|^\xi, \end{aligned} \tag{16}$$

Rescaling the rigidities as

$$k^\alpha_{i,j} = \mathbb{K}^\alpha_e;\ b^\alpha_{i,j} = \mathbb{K}^\alpha_b;\ b^3_{i,j} = \mathbb{K}_p\epsilon^2 \tag{17}$$

and letting $\epsilon \to 0$, the strain energy of the macroscopic system reduces to

$$\begin{aligned} U(\boldsymbol{\chi}(\cdot)) = &\int_\Omega \sum_\alpha \frac{\mathbb{K}^\alpha_e}{2}\|FD_\alpha - 1\|^2 \mathrm{d}S + \\ &+ \int_\Omega \sum_\alpha \frac{\mathbb{K}^\alpha_b}{2}\left[\frac{\|\nabla F|D_\alpha \otimes D_\alpha\|^2}{\|FD_\alpha\|^2} - \left(\frac{FD_\alpha \cdot \nabla F|D_\alpha \otimes D_\alpha}{\|FD_\alpha\|^2}\right)^2\right]\mathrm{d}S + \\ &+ \int_\Omega \frac{\mathbb{K}_p}{2}\left|\arccos\left(\frac{FD_1 \cdot FD_2}{\|FD_1\| \cdot \|FD_2\|}\right) - \frac{\pi}{2}\right|^\xi \mathrm{d}S. \end{aligned} \tag{18}$$

It is noteworthy that the shear strain introduced in the considered macromodel is different from that defined in the Pipkin continuum model (see Equation (8)). In Fig. 15 equilibrium shapes and their corresponding shear strains are compared for different (pure) shear test simulations (refer to problem 2 above) using the strain energy (18). Reference [18] has first addressed the homogenization à la Piola of pantographic fabrics in a linear setting, proving that the homogenization of pantographic fabrics gives rise to second gradient continua. Several numerical simulations show the presence of (internal) boundary layers, a hallmark of second gradient theories. In Fig. 14, numerical simulation of the bias extension test are shown. Colors indicate the shear strain relative to the initial fiber axes (left) and the strain energy density (right) [13]. In Fig. 16, color maps of the strain energy density for standard bias extension test (left) and combined rotation-compression test (right) of a rectangular linear elastic specimen pantographic fabrics with holes are shown.

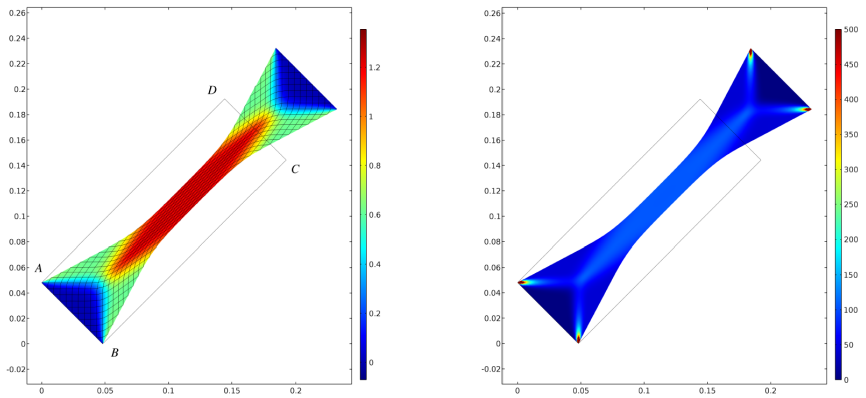

Fig. 14 Numerical simulation of the bias extension test. Colors indicate the shear strain relative to the initial fiber axes (left) and the strain energy density (right) [13].

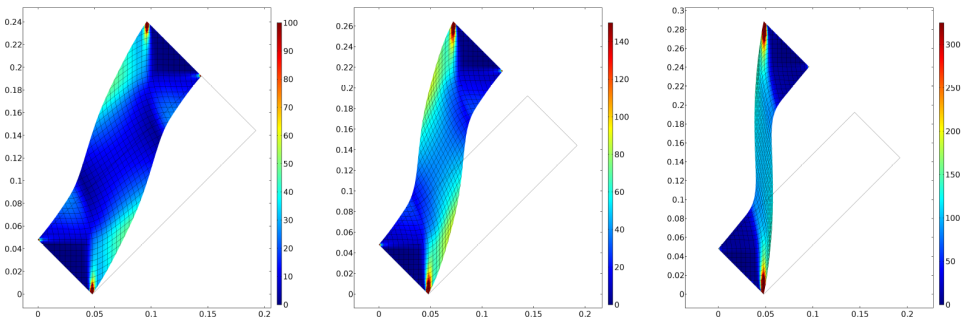

Fig. 15 Equilibrium shape and strain energy density when a shear displacement is prescribed [13].

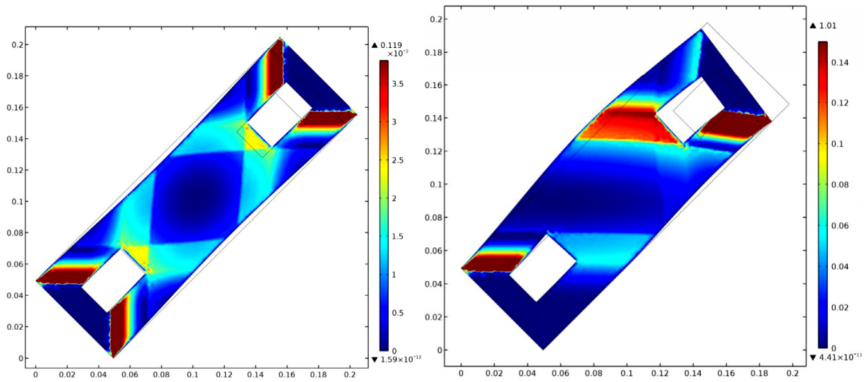

Fig. 16 Color maps of the strain energy density for standard bias extension test (left) and combined rotation-compression test (right) of rectangular linear elastic specimen pantographic fabrics with rectangular holes.

The well-posedness of linearized equilibrium equations deriving from the stationarity of the energy functional (18), which is valid in the neighborhood of a stress free configuration for pantographic sheets, cannot be immediately studied by using the results available in the literature. It has been proven that the standard strategy involving the use of Poincaré inequality, Lax-Milgram Theorem, and coercivity of bilinear strain energy form also apply in the context of linear elastic pantographic sheets [39]. The key idea is the exploitation of an unusual energy space, where the solutions relative to well-posed boundary conditions are looked for. It is observed that the energy space of linear pantographic sheets, i.e. the space of functions fulfilling boundary conditions for which the strain energy is meaningful, is included in a special class of Sobolev spaces, the so-called Anisotropic Sobolev Space. The definition of Anisotropic Sobolev Space was conceived on purely logical grounds by Sergei M. Nikol'skii, and has to be used in order to apply the abstract Hilbertian setting of solution strategy. Thus, in order to address the well-posedness of the planar linearized equilibrium problem for homogenized pantographic lattices, (i) a class of subsets of anisotropic Sobolev space is introduced as the most suitable energy space relative to assigned boundary conditions; (ii) it is proved that the considered strain energy density is coercive and positive definite in such energy space; (iii) the set of placements for which the strain energy is vanishing (the so-called floppy modes) must strictly include rigid motions; (iv) the restrictions on displacement boundary conditions that ensure the existence and uniqueness of linear static problems are determined.

1.5 Numerical identification of homogenized model

In Ref. [37], the parameters $\mathbb{K}_a^\alpha$, $\mathbb{K}_b^\alpha$ and $\mathbb{K}_p$ appearing in the strain energy are assumed to be independent of the position and family of beams they are related to and the strain energy density of the homogenized model (18). The parameter identification is numerical, which means that the constitutive parameters $\mathbb{K}_e$, $\mathbb{K}_b$ and $\mathbb{K}_p$ of the homogenized model are calibrated by means of several numerical computations performed with the 3D Cauchy model of isotropic and homogeneous elastic materials undergoing arbitrarily large strains. Several bias extension test simulations [40] using both the standard Cauchy model and the higher-gradient model, for several displacements prescribed on the shorter side of the specimen, are performed. For each simulation, the overall stored energy and two representative deformations at specific points are evaluated. The two representative deformations are chosen to be the angles ψ_C and ψ_V, evaluated at the probed points shown in Fig. 17, i.e. at the center C of the specimen and at the corner V of the "quasi-rigid" triangle near a base of the specimen.

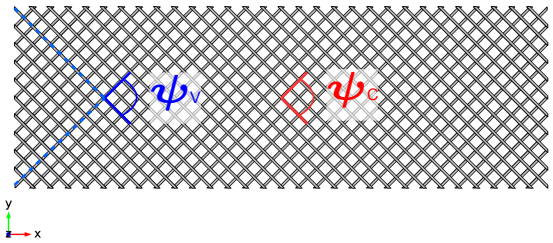

Fig. 17 The two control angles employed in the identification procedure.

The material parameters of the macromodel $\mathbb{K}_e$, $\mathbb{K}_b$ and $\mathbb{K}_p$ are estimated by minimizing the squared errors for the overall stored energy and the two angles ψ_C, ψ_V, when computed both with the homogenized and Cauchy models. The two angles ψ_C, ψ_V have been chosen among other possible control quantities because each of them is strongly related to one of the last two energy terms (18) only dependent only on one parameter each. The energy involved in the distortion angle at the center is mostly governed by the parameter $\mathbb{K}_p$, while the distortion angle at the triangle vertex depends for the most part on the bending energy related to $\mathbb{K}_b$, thus allowing to easily find the minimum of the squared error for the two angles by separately tuning $\mathbb{K}_e$ and $\mathbb{K}_b$. The last parameter $\mathbb{K}_e$ is derived by considering the whole stored energy. In Figs. 18 and 19(left), the total energy and the angles ψ_C and ψ_V used for fitting the second gradient model are shown as the prescribed displacement in the bias extension test is varying. In Fig. 19 (right), a comparison between the total reaction force of the micromodel and the one evaluated with the macromodel is plotted versus the prescribed displacement. This quantity was computed by means of Castigliano's first theorem. Figure 20 shows that for the Cauchy model a non-negligible amount of energy is stored for configurations that are not accounted for in the coarser second gradient model. The main reason is that the Cauchy model has a richer kinematics than the homogenized one. Figure 19(right) confirms this statement that at large displacements, which are likely to be those where strain energies due to the richer kinematics of the refined model start to gain significance.

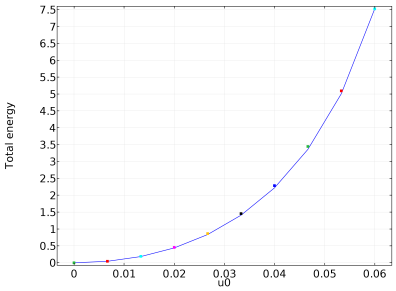

Fig. 18 Comparison of the total energy between the Cauchy model (points) and the second gradient model (solid line).

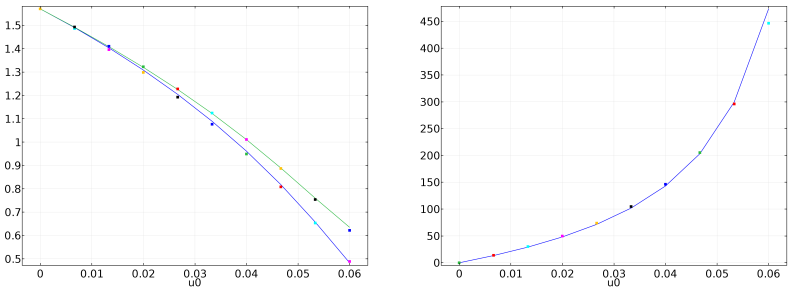

Fig. 19 Comparisons between the Cauchy model (points) and the regression with the second gradient model (solid line). (a) Angle at the center ψ_C (blue line) and angle at the corner ψ_V (green line) on the left; (b) total reaction force.

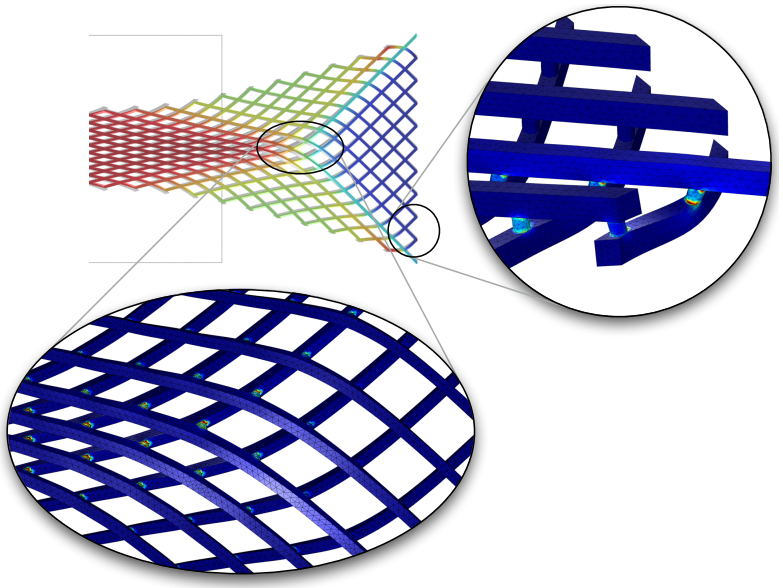

Fig. 20 3D deformation details; the colors in the zooms indicate qualitatively the stored elastic energy density for the 3D Cauchy model.

1.6 Elastic surface models

In Ref. [41], the formulation of a model for pantographic sheets, which is regarded as elastic surfaces embedded in a three dimensional Euclidean space, has been first presented. In order to account for the geodesic (thus generalizing the classical plate theory) and out-of-plane bending of fibers, the model exhibits an associated second-gradient areal strain energy density, which depends on the first and second gradients of the deformation. Accounting for the fact that fibers are arranged in two material directions a Lagrangian Cartesian orthonormal coordinate system, whose associated basis of unit vectors is (D_1, D_2), is introduced in the reference configuration. We now consider a $2D$ continuum, whose reference shape is the rectangular domain $\mathscr{B} \subset \mathbb{R}^2$. As customary, D_1 and D_2 are defined as the push-forward vectors in the current configuration of the vectors D_1 and D_2 respectively, i.e. $D_\alpha = FD_\alpha,\ \alpha = 1, 2$. In the sequel fiber stretches $\|D_\alpha\|$ are denoted as λ and μ

$$F = D_1 \otimes D_1 + D_2 \otimes D_2 = \lambda \tilde{D}_1 \otimes D_1 + \mu \tilde{D}_2 \otimes D_2 \tag{19}$$

where $\tilde{D}_\alpha = \frac{D_\alpha}{\|D_\alpha\|}$ are the unit vectors associated with D_α. Such vectors are used to define the fiber shear strain γ as $\sin\gamma = \tilde{D}_1 \cdot \tilde{D}_2$ [13,41]. The shear strain introduced in this model is different from that defined in the Pipkin continuum model [10,35,34]. From Equation (19) the right Cauchy-Green tensor reads

$$C = F^{\mathsf{T}}F = \lambda^2 D_1 \otimes D_1 + \mu^2 D_2 \otimes D_2 + \lambda\mu \sin\gamma \left(D_1 \otimes D_2 + D_2 \otimes D_1\right). \tag{20}$$

and

$$Jn = FD_1 \times FD_2 = D_1 \times D_2 \tag{21}$$

with n the unit normal of the deformed surface field, and $J = \lambda\mu|\cos\gamma|$ the local areal dilation due to the deformation. In [41] the following representation formula is proven

$$\nabla\nabla\boldsymbol{\chi} = (g_1 + K_1 n) \otimes D_1 \otimes D_1 + (g_2 + K_2 n) \otimes D_2 \otimes D_2 + (\boldsymbol{\Gamma} + Tn) \otimes (D_1 \otimes D_2 + D_2 \otimes D_1) \tag{22}$$

with

$$g_1 = \lambda\eta_1 p + (D_1 \cdot \nabla\lambda)\,\tilde{D}_1;\ g_2 = \mu\eta_2 q + (D_2 \cdot \nabla\mu)\,\tilde{D}_2 \tag{23}$$

$$\boldsymbol{\Gamma} = (D_1 \cdot \nabla\mu)\,\tilde{D}_2 + \lambda\mu\phi_1 q = (D_2 \cdot \nabla\lambda)\,\tilde{D}_1 + \lambda\mu\phi_2 p \tag{24}$$

$$q = n \times \tilde{D}_2;\ p = n \times \tilde{D}_1 \tag{25}$$

$$K_1 = \lambda^2\kappa_1;\ K_2 = \mu^2\kappa_2;\ T = \lambda\mu\tau. \tag{26}$$

The quantities η_1 and η_2 in (23) are the geodesic curvatures of the deformed fibers, ϕ_1 and ϕ_2 appearing in (24) are the so-called Tchebychev curvatures, κ_1 and κ_2 appearing in (26) are the normal curvatures of the deformed fibers and τ measures the twist of the deformed surface. In [41] explicit expressions for geodesic and Tchebychev curvatures are provided and we have

$$\begin{aligned}
J\eta_1 &= D_1 \cdot \nabla(\mu \sin\gamma) - D_2 \cdot \nabla\lambda \\
J\eta_2 &= D_1 \cdot \nabla(\mu) - D_2 \cdot \nabla(\lambda \sin\gamma) \\
J\phi_1 &= J\eta_2 + \lambda D_2 \cdot \nabla(\sin\gamma) \\
J\phi_2 &= J\eta_1 + \mu D_1 \cdot \nabla(\sin\gamma).
\end{aligned}$$

Furthermore, a strain energy density function, which depends on the first and second gradients of the deformation and incorporating the orthotropic symmetry conferred by the reference fiber arrangement, is proposed in [42]

$$W = w(\lambda, \mu, J) + \frac{1}{2}\left(A_1|g_1|^2 + A_2|g_2|^2 + A_\Gamma|\boldsymbol{\Gamma}|^2 + k_1K_1^2 + k_2K_2^2 + k_TK_T^2\right) \tag{27}$$

where A_1, A_2, A_Γ, k_1, k_2, k_T are constitutive constants. In Fig. 21 numerical simulation of torsion of a square sheet using the elastic surface model presented above is shown. Using the above model, many fiber reference curvatures have been considered (e.g. sinusoidal, spiral, parabolic fibers) and, for parabolic fibers, experiments (Fig. 22) and model (Fig. 23) both show that, after a critical loading, out-of-plane buckling occurs during bias extension, because the transverse (curved) beams in the middle of the specimen undergo buckling induced by the shortening of the middle width of the specimen.

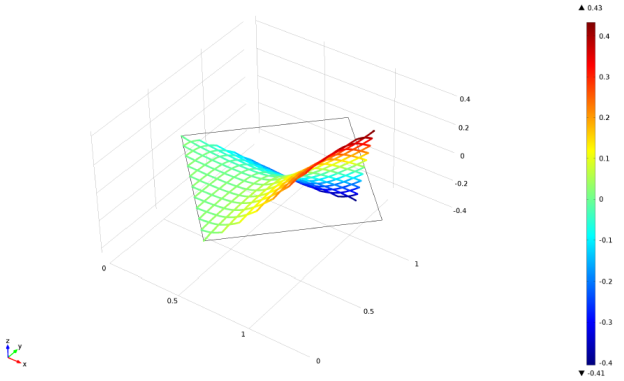

Fig. 21 Numerical simulation of torsion of a square sheet ($\theta = 60°$) using the elastic surface model presented above. Colors represent qualitatively the out-of-plane component of the displacement u_3.

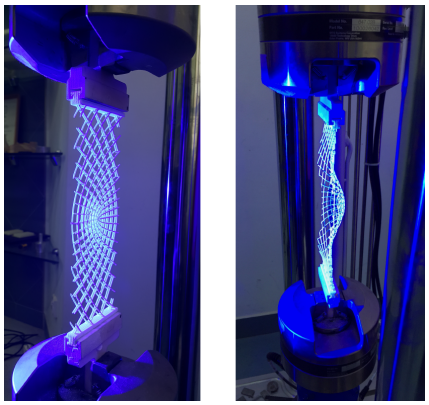

Fig. 22 Bias extension test on parabolic pantographic fabric. Out-of-plane buckling is observed after critical loading.

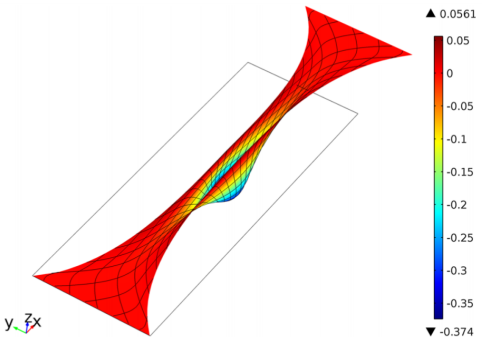

Fig. 23 Simulation of bias extension test on parabolic pantographic fabrics. Out-of-plane buckling is observed after a critical loading. Deformed configuration and qualitative out of plane displacement.

A 2D continuum model embedded in a 3D space has been also proposed [43] where, relying on a variational framework, the following strain energy density is proposed

$$\pi = \frac{1}{2}\left\{ \mathrm{K}_e \left[\left(\epsilon^1\right)^2 + \left(\epsilon^2\right)^2 \right] + \mathrm{K}_s \gamma^2 + \right. \\ \left. + \mathrm{K}_t \left[\left(\kappa_1^1\right)^2 + \left(\kappa_1^2\right)^2 \right] + \mathrm{K}_n \left[\left(\kappa_2^1\right)^2 + \left(\kappa_2^2\right)^2 \right] + \mathrm{K}_g \left[\left(\kappa_3^1\right)^2 + \left(\kappa_3^2\right)^2 \right] \right\} \tag{28}$$

It corresponds to a system of two orthogonal continuous families "1" and "2" of straight shear-undeformable beams arranged along the coordinate axes in the reference configuration and resembling the pantographic microstructure. The fibers of family α are parallel to the direction $\hat{e}_\alpha$. The contributions $\frac{1}{2}\mathrm{K}_e \left(\epsilon^1\right)^2$ and $\frac{1}{2}\mathrm{K}_e \left(\epsilon^2\right)^2$ stand for the elongation of fibers belonging to, respectively, the families "1" and "2." The strain measure $\boldsymbol{\epsilon}^\alpha$, with $\alpha = 1, 2$, is defined as

$$\epsilon^\alpha = \left\| \frac{\partial \chi}{\partial X_\alpha} \right\| - 1 \tag{29}$$

and $\mathrm{K}_e \in [0, \infty)$ is the corresponding stiffness, which is assumed to be the same for both families of fibers. The contribution $\mathrm{K}_s \gamma^2$ is accounting for the shear deformation of the sheet, i.e. it is due to the relative rotation of two orthogonal intersecting fibers. It represents the strain energy stored in the pivot because of its torsion of angle γ. The strain measure $\gamma \in [-\frac{\pi}{2}, \frac{\pi}{2}]$, also referred to as the shear angle, is defined as

$$\gamma = \arcsin \frac{\frac{\partial \chi}{\partial X_1} \cdot \frac{\partial \chi}{\partial X_2}}{\left\| \frac{\partial \chi}{\partial X_1} \right\| \left\| \frac{\partial \chi}{\partial X_2} \right\|} \tag{30}$$

and K_s, m and Q are positive constitutive parameters. The terms $\frac{1}{2}\left[\mathrm{K}_t \left(\kappa_1^1\right)^2 + \mathrm{K}_n \left(\kappa_2^1\right)^2 + \mathrm{K}_g \left(\kappa_3^1\right)^2\right]$ and $\frac{1}{2}\left[\mathrm{K}_t \left(\kappa_1^2\right)^2 + \mathrm{K}_n \left(\kappa_2^2\right)^2 + \mathrm{K}_g \left(\kappa_3^2\right)^2\right]$ are due to twist, normal bending and geodesic bending of beams belonging, respectively, to families "1" and "2" of fibers. The strain measures κ_1^α, κ_2^α, κ_3^α are the coordinates, in the augmented levorotatory reference Cartesian frame, of the axial vector corresponding to the skew tensor $W^\alpha = (R^\alpha)^{\mathrm{T}} \frac{\partial R^\alpha}{\partial X_\alpha}$, which is the so-called current curvature tensor. The orthogonal tensor R^α transforms the augmented levorotatory reference Cartesian frame vectors into the following ordered triplet: i) the unitary vector tangent to the deformed coordinate line α; ii) the unitary vector normal to the previous one and lying in the plane tangent to the deformed surface; iii) the unitary vector normal to the plane tangent to the deformed surface. Explicit (lengthy) derivations can be found in Ref. [43].

It is worth noting that i) since the beams are assumed to be shear-undeformable ii) both R^1 and R^2 transform the third vector $\hat{e}_3$ of the augmented levorotatory reference Cartesian frame into the same vector, iii) assuming that principal inertia axes of the cross-sections for the two families "1" and "2" of beams in the undeformed configuration are considered to be respectively $(\hat{e}_2, \hat{e}_3)$ and $(-\hat{e}_1, \hat{e}_3)$, the cross-sections of the beams belonging to the two families "1" and "2" are eigen inertia vectors in the deformed configuration the unitary vectors of points ii) and iii) above and, hence, they share the second principal inertia axis at point iii) above. Such vector can be interpreted also as the current axis of the elastic cylindrical pivot. This means that deformation modes of the pivots other than their torsion are kinematically excluded in this model, i.e. the pivots are assumed to remain orthogonal to both fibers in the current configuration and only their torsion contributes to the strain energy. Further, κ_1^α, κ_2^α, κ_3^α can also be interpreted as geodesic torsion, normal curvature and geodesic curvature of the deformed surface multiplied respectively by $\|\frac{\partial \chi}{\partial X_\alpha}\|$, since X_α is not a unitary speed parameterization. Last, the fibers intersecting in one point cannot detach or have a relative displacement, since their motion is described by the same placement function (this is not a so-called mixture model). Using the above model shear test simulations have been performed reporting the occurrence of out-of-plane buckling (Fig. 24).

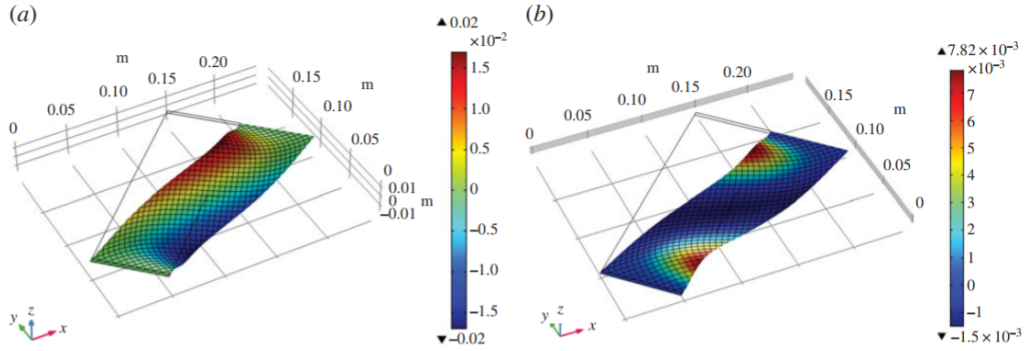

Fig. 24 Shear test. Qualitative buckled shapes of the first two bifurcation modes. Colors indicate values of the out-of-plane displacement. (a) First and (b) second buckling modes.

1.7 Analytical identification of elastic plate models

Let us consider a 2-dimensional body, whose points can be put in a bijective correspondence with a closed subset $\mathcal{B}$ of the Euclidean space $\mathbb{R}^2$. The set $\mathcal{B}$ represents the shape of the body in the reference (undeformed) configuration. A Cartesian coordinate system $(\mathcal{O}, (\hat{e}_1, \hat{e}_2))$ is introduced, with $X = (X_1, X_2)$ the coordinates of the generic point in the Euclidean space $\mathbb{R}^2$. Working in a Lagrangian framework, a placement function $\chi : \mathcal{B}_0 \to \mathbb{R}^2$ such that the image $x = \chi(X)$ of X through χ is the current position of point X. The displacement field $u : \mathcal{B}_0 \to \mathbb{R}^2$ is defined as $u(X) = \chi(X) - X$. The placement, or equivalently the displacement, is the independent kinematic descriptor of the system. The image $\mathcal{B} = \chi(\mathcal{B})$ of $\mathcal{B}$ through χ is the current shape of the body. Let $F = \nabla_X \chi$ be the gradient (with respect to the Lagrangian coordinate X) of the placement function χ. The tensor F belongs to Lin^+, the group of second order tensors with positive determinant i.e. orientation preserving. An objective strain measure $G = \left[F^T F - I\right]/2$ (Green-Lagrange strain tensor) is then defined. Henceforth, the subscript X will be omitted in ∇_X and each space derivative will be considered a material derivative. When the strain energy density $\hat{U}(G, \nabla G)$ is considered to be depending quadratically upon the deformation tensor G and its gradient ∇G, the following representation formula applies [44]

$$\hat{U}^{strain} = \frac{1}{2}\epsilon^T C_{3\times 3}\epsilon + \frac{1}{2}\eta^T A_{6\times 6}\eta \tag{31}$$

with

$$\epsilon = \left(G_{11}\ G_{22}\ \sqrt{2}G_{12}\right)^T \tag{32}$$

and

$$\eta = \left(G_{11,1}\ G_{22,1}\ \sqrt{2}G_{12,2}\ G_{22,2}\ G_{11,2}\ \sqrt{2}G_{12,1}\right)^T \tag{33}$$

In order to account for anisotropy of the material, we must assume invariance of the strain energy density under the action, on the Cartesian coordinate system $\mathcal{O}, (\hat{e}_1, \hat{e}_2)$ labelling points of the reference configuration, of some symmetry group S of transformations, which could be any subgroup of *Orth*. When the symmetry group is the dihedral group D4 (orthotropic material) we have the following representations for the matrices $C_{3\times 3}$ and $A_{6\times 6}$

$$C^{D4}_{3\times 3} = \begin{pmatrix} c_{11} & c_{12} & 0 \\ c_{12} & c_{22} & 0 \\ 0 & 0 & c_{33} \end{pmatrix} \tag{34}$$

and

$$A^{D4}_{6\times 6} = \begin{pmatrix} A^{D4}_{3\times 3} & 0 \\ 0 & A^{D4}_{3\times 3} \end{pmatrix} \tag{35}$$

with c_{11} and c_{12} in $C^{D4}_{3\times 3}$ corresponding to the two Lamé coefficients

$$A^{D4}_{3\times 3} = \begin{pmatrix} a_{11} & a_{12} & a_{13} \\ a_{12} & a_{22} & a_{23} \\ a_{13} & a_{23} & a_{33} \end{pmatrix} \tag{36}$$

In Refs. [45–47] compatible identifications of the constitutive parameters appearing in Equation (31) have been carried out, thus completely characterizing the set of constitutive parameters in terms of the fiber base material parameters (i.e. Young's modulus), of the fiber cross-section parameters (i.e. area and moment of inertia), and of the distance between the nearest pivots. In particular, the constitutive parameters have been identified in the small strain case $|\nabla u| \ll 1$, modeling fibers as (geometrically linear) Euler-Bernoulli beams and pivots as rotational (elastic) springs with a quadratic potential in the relative rotation (torsion of pivots) angle between fibers belonging to two different families. The following expressions for the matrices $C^{D4}_{3\times 3}$ and $A^{D4}_{3\times 3}$ are the outcome of the investigation [47]

$$C^{D4}_{3\times 3} = \begin{pmatrix} \frac{EA}{d} & 0 & 0 \\ 0 & \frac{EA}{d} & 0 \\ 0 & 0 & 2k_R \end{pmatrix} \tag{37}$$

$$A^{D4}_{3\times 3} = \frac{EI}{d} \begin{pmatrix} 0 & 0 & 0 \\ 0 & 1 & -\sqrt{2} \\ 0 & -\sqrt{2} & 2 \end{pmatrix} \tag{38}$$

with E, A and I being, respectively, the Young's modulus, the cross-sectional area and the inertia moment of the cross-section of beams, and d being the spacing between adjacent beams. Finally, k_R is the equivalent elastic torsional stiffness of the cylindrical pivots. The shear strain relative to the directions v and w is defined as (with $-\frac{\pi}{2} < \gamma < \frac{\pi}{2}$)

$$\sin\gamma = \cos\left(\frac{\pi}{2} - \gamma\right) = \frac{Fv \cdot Fw}{\|Fv\|\,\|Fw\|} = \frac{w^T F^T F v}{\|Fv\|\,\|Fw\|} = \frac{w^T\,(2G+I)\,v}{\|Fv\|\,\|Fw\|}. \tag{39}$$

In the present case $w = \hat{e}_1$ and $v = \hat{e}_2$. Thus, assuming that $-\frac{\pi}{2} \leq \gamma \leq \frac{\pi}{2}$

$$\gamma = \arcsin\left(\frac{2G_{12}}{\sqrt{(1+u_{1,1})^2 + u_{2,1}^2}\,\sqrt{(1+u_{2,2})^2 + u_{1,2}^2}}\right). \tag{40}$$

In the case of small strains, i.e. geometrically linear case $|\nabla u| \ll 1$

$$\gamma \simeq \arcsin\left(u_{1,2} + u_{2,1}\right) \simeq u_{1,2} + u_{2,1}. \tag{41}$$

Equation (31) yields the following remarkable expression for the strain energy density

$$\hat{U}^{strain} = \underbrace{\frac{1}{2}k_R\left(u_{1,2}+u_{2,1}\right)^2}_{\text{shear (pivot torsion) contribution}} + \underbrace{\frac{EA}{2d}\left(u_{1,1}^2 + u_{2,2}^2\right)}_{\text{extension of fibers}} + \underbrace{\frac{EI}{2d}\left(u_{1,22}^2 + u_{2,11}^2\right)}_{\text{bending of fibers}} \tag{42}$$

In Ref. [45], numerical solutions using the strain energy density (42) are presented for a circular pantographic specimen and three exemplary problems: bias extension, shear, and rotation tests (Fig. 25).

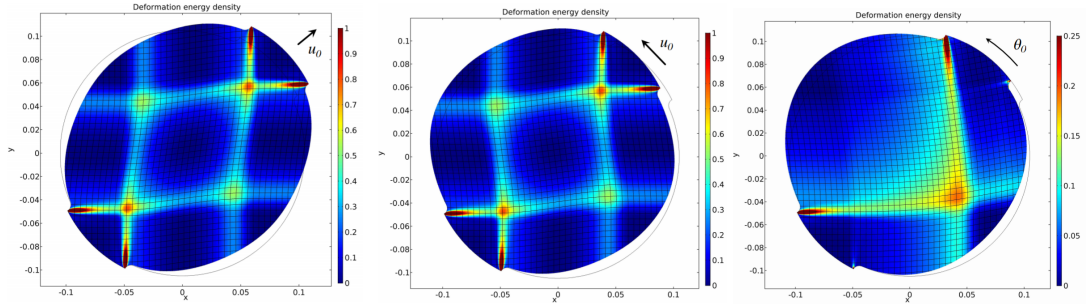

(a) (b) (c)

Fig. 25 Circular pantographic specimen. Qualitative color maps of the strain energy density for: bias extension test (a), shear test (b), rotation test (c).

In Ref. [48], two pantographic sheets with an aspect ratio 3:1 are considered, having i) the same fiber directions and ii) a part of their common sides interconnected by terminal clamping constraints, i.e. the displacements in the interconnected regions are point-wise equal for the two pantographic sheets. In the region corresponding to the cut separating the two sheets, no kinematic constraint is assumed for their relative displacement and the results shown in Fig. 26 are obtained for a standard bias extension test. Pantographic sheets without any internal cut are considered as well, see Fig. 27, where Eulerian representations of the strain energy densities are given for two non-standard bias extension tests and in presence (absence) of the shear energy contribution. In particular in the first (higher) two plots in Fig. 27 the left side of the specimen has been clamped and the other sides are free, while the vertices of the right side are displaced along the direction of the longer sides. Instead, in the lower two plots, the left side of the specimen has been clamped and the lower half of the right side has been displaced along the direction of the longer sides, while the remaining boundaries are free. Second gradient energies allow for external actions on 2D continua not only on edges, but also on vertices, as vertex boundary conditions and vertex-forces.

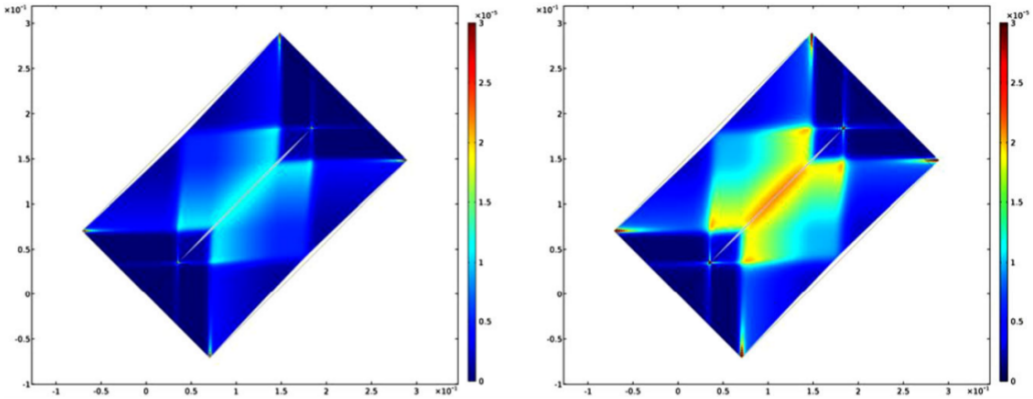

Fig. 26 Effect of a cut inside a sheet. Eulerian representation of the elastically stored energy density for a sheet with lower shear stiffness (left) and for a sheet with higher shear stiffness (right), both subject to a standard bias extension test.

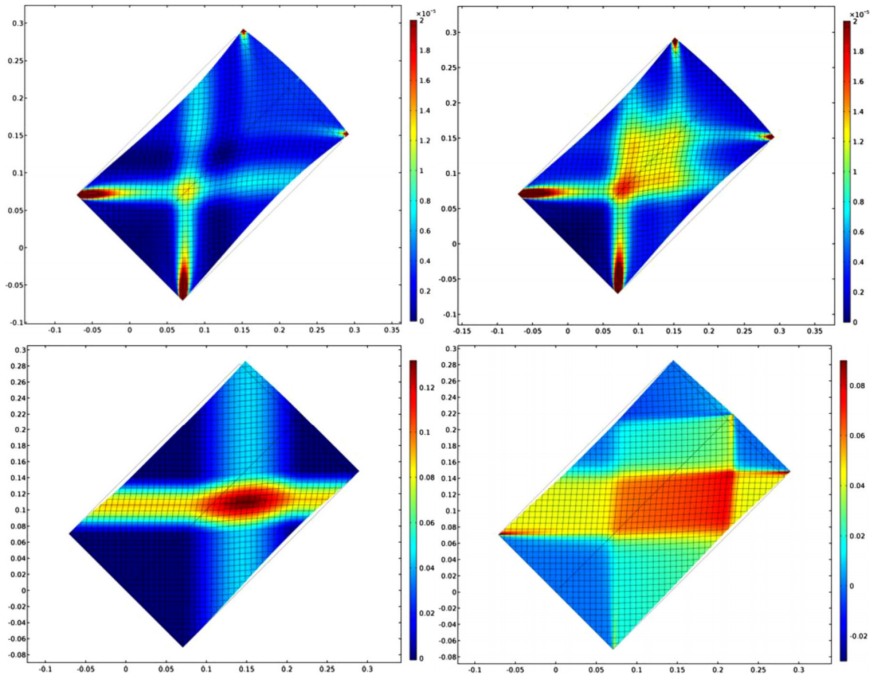

Fig. 27 Non-standard bias extension test: Eulerian representation (including deformed shape and deformed sampled material lines) of the strain energy density for a sheet whose expression does not include the shear contribution (left) and for a sheet whose strain energy includes the shear contribution (right).

1.8 Wave propagation in discrete arrangements of Euler beams

In Ref. [49], a model for studying the dynamics of pantographic fabrics has been introduced and subsequently employed [50,51]. Pantographic rectangular "long" wave-guides are studied and time-dependent boundary displacements inducing the onset of travelling waves are considered. In this model the two families of orthogonal fibers are regarded as two families of $1D$ orthogonal straight continua arranged in a rectangle in the reference configuration. Each continuum $\mathcal{C}_i$ has a standard linearized Euler elastic potential given by

$$U_i = \frac{1}{2}\int_{\mathcal{C}_i} k_M \left(u''(s)\right)^2 + k_N \left(w'(s)\right)^2 \mathrm{d}s \tag{43}$$

with s an abscissa introduced on each $\mathcal{C}_i$, k_M the bending stiffness, k_N the axial stiffness, u and w, respectively, the transverse and axial displacements. Dots in Fig. 28(left) indicate the presence of frictionless hinges that do not interrupt the continuity of the beams. The displacement prescribed on the structure is an impulse function $\mathfrak{I} = u_0 * \mathrm{sech}\left[\tau(t - t_0)\right]$, with τ being a parameter affecting the duration of the pulse (Fig. 28(right)).

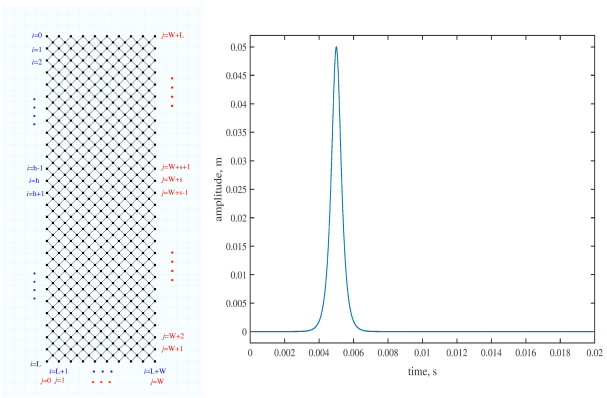

Fig. 28 Reference configuration (left) and time history of the impulse (right).

In Fig. 29(left) plots of the deformed shape of a pantographic strip during the propagation of a wave generated by a vertical impulse, uniformly applied on the upper side of the specimen while its lower side remains clamped, are shown. Colors represent the magnitude of the total rotation of the cross section of the beams. In Fig. 29(right) plots of the deformed shape of a pantographic strip during the propagation of a wave, generated by a double impulse applied at the middle height of the specimen, are shown, along with colors representing the magnitude of the total rotation of the cross section of the beams. By double impulse we mean a couple of displacements, having the same orientation but opposite directions, oriented in one of the two orthogonal characteristic directions of the pantographic sheet. Such displacements are prescribed on two points at the opposite ends of two adjacent beams, i.e consecutive beams belonging to the same orthogonal family of $1D$ continua, and their amplitude over time is shown in Fig. 28.

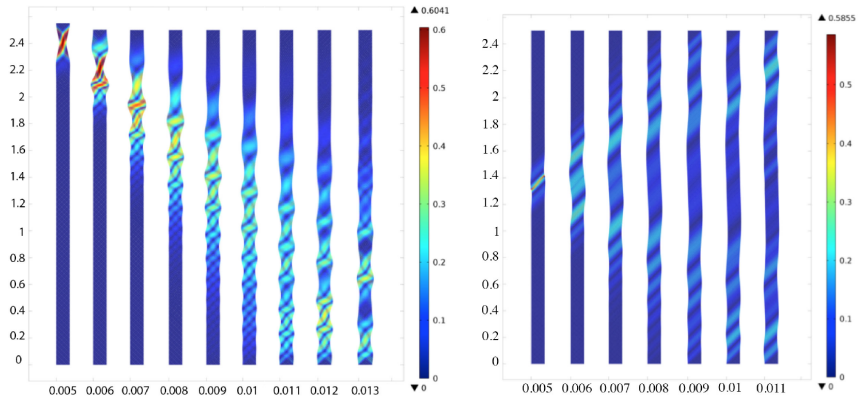

Fig. 29 Qualitative displacement plot of a wave propagating after a prescribed vertical displacement on the upper side (left). Wave propagating after double impulse (right).

Such a double impulse corresponds, in the continuous homogenized limit case, to a double force, i.e. to a pair of forces with null resultant and moment. Since such a kind of forces can not be included in a first gradient continuum theory, in order to capture with a continuum model the dynamic features shown in Fig. 28, one has to move to second gradient theories. Figure 30 shows

that the energy of the system remains substantially confined in the upper half of the wave-guide and propagation of waves beyond the discontinuity is negligible. Therefore, such type of discontinued pantographic structures induces damping.

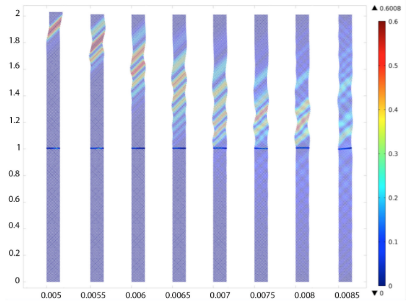

Fig. 30 Qualitative displacement of wave propagation in two identical lattices connected by an array of vertical beams.

2 Damage and failure in pantographic fabrics

So far the study of damage mechanisms in pantographic fabrics has been addressed from a modelling standpoint [52,53]. Further experimental data can be found [10,54]. In Ref. [52], in the aforementioned discrete quasi-static Hencky spring model (Section 1.3) a simple irreversible rupture mechanisms is considered for the springs. A spring is ruptured if its strain level exceeds (upper threshold) or is less than (lower threshold) a certain (constant) threshold. In particular, the criterion for rupture of a spring at iteration t, which discriminates whether that spring has to be removed from the computations at iteration $t+1$ or not, is based on (constant) thresholds for the relative elongation of extensional springs like, e.g., $(\|p_{i+1,j} - p_{i,j}\| - \epsilon)$ (upper and lower thresholds are employed for this deformation measure). Upper thresholds for the relative rotation of adjacent springs belonging to the same fiber like, e.g., $\left(\cos \vartheta^1_{i,j} + 1\right)$ and for the relative rotation of adjacent springs belonging to different fibers like $\left|\vartheta^3_{i,j} - \frac{\pi}{2}\right|$ are contemplated but are not considered. Indeed, since the analyzed pantographic sheet is made out of a ductile material (polyamide), damage is governed by fiber breakage due to excessive extension, rather than fiber breakage due to excessive bending or pivot failure due to torsion.

This is an experimental evidence [10], where displacement-controlled uniaxial bias extension tests (Fig. 31) were performed on three different polyamide specimens and the first failure event was observed at the corners of the specimen, where elongation of fibers is the highest.

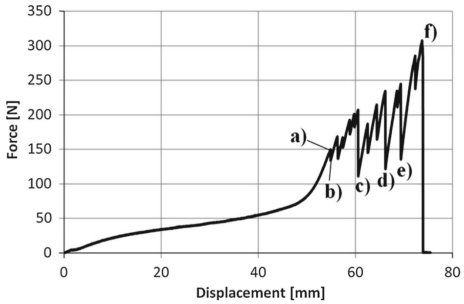

Fig. 31 Force versus prescribed displacement for a uniaxial bias extension test. (a) Sample before first beam breakage (i.e. breakdown onset); (b) upper-left corner beam breakage; (c)-(f) further fiber breakage.

This evidence is confirmed, through a different test [52] (see Fig. 32), since fiber elongation is the highest at the lower-left and upper-right corners. When the sample is made out of a brittle material, damage is governed by excessive shear strains (i.e. torsion of pivots) that, in the displacement-controlled uniaxial bias extension test, reaches its maximum near the two internal vertices of the quasi-rigidly deforming triangles.

(a) (b)

Fig. 32 (a) Reference configuration ($\lambda = 0$), (b) damage onset ($\lambda = 0.976$) of a shear test.

In Ref. [52], a slow-rate (15 mm/min) uniform horizontal displacement on the top of the specimen is prescribed. The prescribed horizontal displacement $\overline{u}$ and the corresponding non-dimensional displacement λ are the prescribed quantities. First fiber breakage is observed for a horizontal displacement $\overline{u} = 139.96$ mm (Fig. 32), which corresponds to a non-dimensional displacement $\lambda = 0.976$. By comparing Figs. 32 and 34, the model correctly predicts the location of fiber breakage. The "generalized" (because of the introduction of damage) numerical model fits well the force-displacement curve throughout the experiment, up to the onset of fiber breakage (Fig. 33).

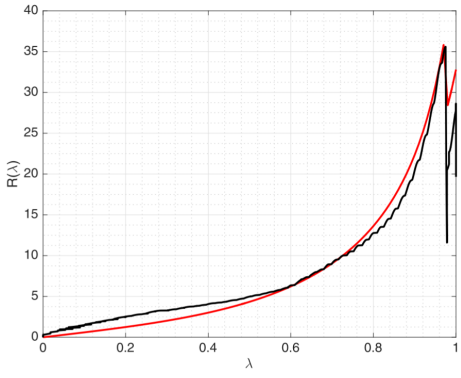

Fig. 33 Force (N) vs non-dimensional displacement for the shear test of a pantographic sheet up to the onset of fiber breakage. The black curve is the experimental data, and the red curve has been obtained via numerical simulation.

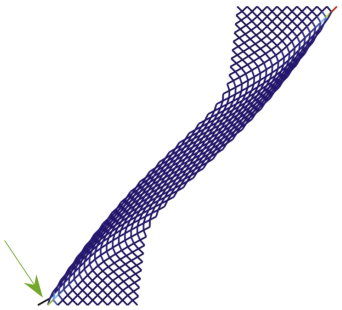

Fig. 34 Deformed configuration at the onset of damage. The broken fiber is colored in black and it is pointed by the green arrow.

In Ref. [53], pivot damage due to shear, i.e. fibers detaching due to friction in pivots, is taken into account, thereby allowing for sliding between the two families of fibers. Thus, the nonlinear homogenized quasi-static model for the discrete system in Fig. 11 (for more details about the homogenization procedure the reader is referred to Ref. [13] is modified by introducing, in the spirit of mixture theory, two independent placement functions χ^1 and χ^2 (the placement functions of body points belonging to horizontal and vertical fibers, respectively) defined on the same reference domain and, accordingly, considering the following nonlinear (elastic) strain energy to be minimized at each iteration

$$\int_{\mathcal{B}_0} \underbrace{\sum_{\alpha=1,2} \frac{K_e^\alpha}{2} \|F^\alpha \hat{e}_\alpha - 1\|^2}_{\text{extension of horiz. and vert. fibers}} + \int_{\mathcal{B}_0} \underbrace{\frac{K_p}{2} \left| \arccos\left(\frac{F^1\hat{e}_1 \cdot F^2\hat{e}_2}{\|F^1\hat{e}_1\| \cdot \|F^2\hat{e}_2\|} \right) - \frac{\pi}{2} \right|^\xi}_{\text{shear (pivots torsion) contribution}} + \tag{44}$$

$$\int_{\mathcal{B}_0} \underbrace{\sum_{\alpha=1,2} \frac{K_b^\alpha}{2} \left[\frac{\|\nabla F^\alpha |\hat{e}_\alpha \otimes \hat{e}_\alpha\|^2}{\|F^\alpha \hat{e}_\alpha\|^2} - \left(\frac{F^\alpha \hat{e}_\alpha \cdot \nabla F^\alpha |\hat{e}_\alpha \otimes \hat{e}_\alpha}{\|F^\alpha \hat{e}_\alpha\|^2} \right)^2 \right]}_{\text{bending of horiz. and vert. fibers}} + \int_{\mathcal{B}_0} \underbrace{\frac{K_{int}}{2} \|\chi^1 - \chi^2\|^2}_{\text{relative sliding of the two layers}} \tag{45}$$

In Ref. [53] relative sliding of two families) evolves following a criterion based on thresholds for the relative distance $\delta = \|\chi^1 - \chi^2\|$ between χ^1 and χ^2 (e.g., the fitted K_{int} in Fig. 35.

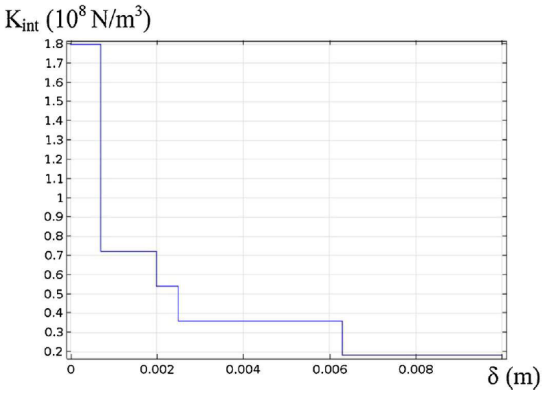

Fig. 35 Dependence of the resistance to sliding K_{int} on δ.

A numerical example where an aluminum specimen is subject to uniaxial bias extension is shown. Constitutive parameters K_e^α, K_b^α, K_p and K_{int} were fitted using experimental data (Fig. 36), showing a very good agreement. The experiment is studied only up to the first rupture (i.e. as long as $K_{int} > 0 \ \forall X \in \mathcal{B}_0$). For the discrete model [52], and in turn for the continuum homogenized model [53] (as for their respective purely elastic counterparts), it is straightforward to implement the case of non-orthogonal initially straight fibers [55].

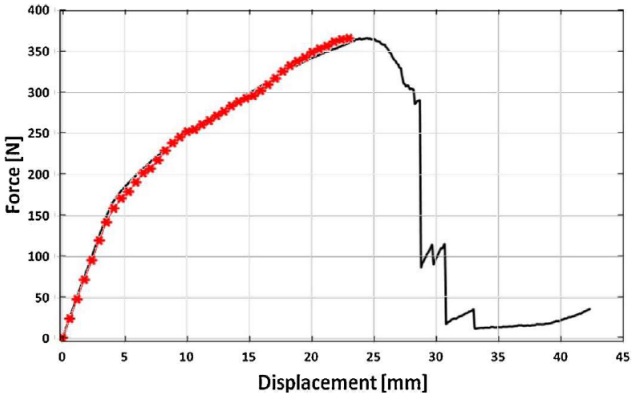

Fig. 36 Force vs. applied displacement for a uniaxial bias extension test of an aluminum pantographic sheet. The black curve is the experimental measurement and the red obtained via numerical simulation.

Further, the two models have been extensively tested when dealing with pure (nonlinear) elasticity, and they show a nearly perfect agreement with experimental results. In Fig. 37(b), the onset of damage is observed at the upper-left corner beam only. This is due to undesired asymmetries in the experimental setup (e.g. specimen, loading, clamping).

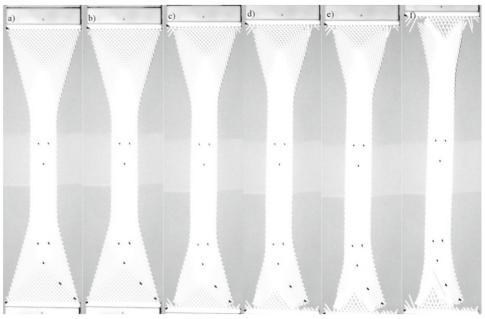

Fig. 37 A sample subject to uniaxial bias extension. (a) sample before the first beam breakage (i.e. breakdown onset); (b) upper-left corner beam rupture; (c)–(f) rupture of further fibers.

3 Feasibility of digital image correlation analyses

Up to now, the only kinematic data that were reported were prescribed macro-displacements or discrete measurements (e.g. control angles, see Fig. 17). In the future is is desirable to have a richer experimental data base to calibrate and validate in a more extensive way the discussed models. In the following, the feasibility of performing displacement field measurements on pantographic

samples is assessed. Since very large displacement levels occur, digital image correlation (DIC [56, 57]) has been selected. In the case study reported hereafter, a series of 42 pictures was acquired with an 8-bit digitization, and 1944×2592-pixel definition camera. Gray level images are reconstructed by a binning of two processes to account for Bayer (color) filter. They are subsequently cropped, so that their final definition is 1147×261 pixels. For DIC purposes, the upper and lower parts of the grips were speckled (Fig. 38). In addition, the hinges of the pantographic sheet were marked in black, and a red background was used in order to create high contrast with the white color of pantographic sheet.

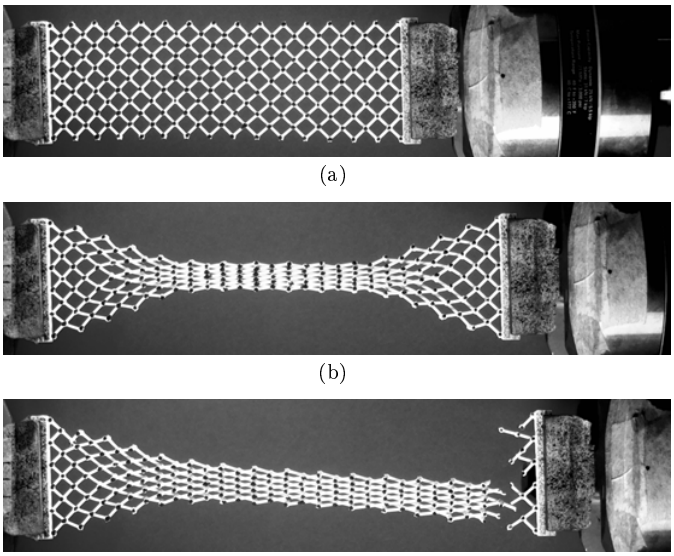

(a) (b) (c)

Fig. 38 Gray level images of the pantograph in the reference configuration (a), last analyzed deformed configuration (b), and at failure (c).

The analysis of the motions of the pantographic sheets can be performed at different scales. The most logical, yet the most difficult, would have been to have a geometric description fitting the actual shape of the pantographic fabric and measure the displacements at the corresponding discretization level (i.e., as in the 3D Cauchy model, see Fig. 20). One challenge is to measure surface displacements with such fine meshes since each element will very few pixels. This would clearly require regularizations to be considered [58]. Integrated approaches may also be considered in which the displacement fields are derived thanks to numerical simulations [59]. Another option would be consider the kinematics of beams (e.g. with Euler-Bernoulli kinematics). DIC analyses may then be easier since the number of degrees of freedom could be significantly reduced [60]. In the present case, this would have meant having an explicit description of all the struts composing the pantographic fabric. Another path consists in measuring macroscopic motions via so-called local or global DIC [61]. Since the final aim of such analyses is their comparison with numerical simulations, the displacement fields will be expressed in the same language of the results obtained by numerical simulations, namely, with finite element bases. Global DIC with 3-noded triangles and with linear interpolation functions is here considered (i.e. T3-DIC). Since the mesh is not compatible with the pantograph mesostructure, mechanical regularization will be used to enable the DIC code to converge (i.e. RT3-DIC [58]). In order to avoid any significant bias, the regularization length is identical to the element length (i.e. 25 pixels in the present case). Figure 39(a) shows the region

of interest (ROI) that extends over the whole pantographic sheet and over part of the speckled grips. This setting allows the RT3-DIC code to converge first in the grips and then in the central part of the pantographic sheet, where most of the deformation takes place. In the present case, the convergence criterion was set to 10^{-5} pixel for the norm of the mean displacement corrections. This very low value could be achieved thanks to the employed regularization strategy.

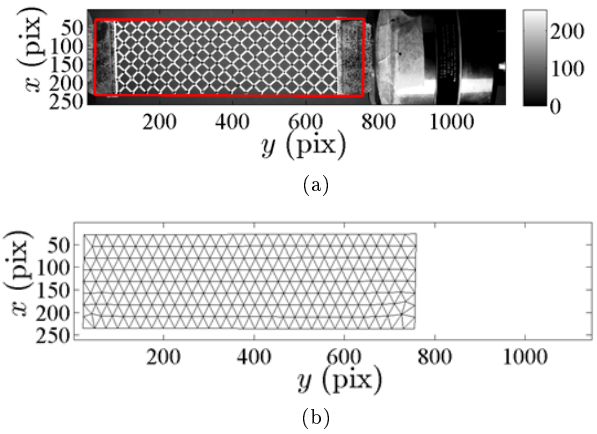

Fig. 39 (a) Region of interest (red box) analyzed via RT3-DIC. (b) Finite element mesh with 25-pixel T3 elements.

Figure 40 shows the results of the RT3-DIC analysis of the 5th loading step. First, the gray level residuals are being checked (Fig. 40(a)). They correspond to the gray level differences between that in the picture in the reference configuration and that in the deformed configuration corrected by the measured displacement field. If perfect match were achieved, this difference would only contain acquisition noise. This is not observed in the present case, since there still are some stigmata of the pantographic sheet geometry. It confirms that a continuous kinematic basis made of 3-noded triangles cannot fully capture the present kinematics. However, the deviations remain very small. Consequently, the displacement fields shown in Fig. 40(b-c) are deemed trustworthy at the macroscale. The transverse displacement field u_x shows that there is a huge contraction in comparison with the longitudinal motions u_y. This is due to the geometry of the pantographic sheet. This observation translates into the nominal strain components reported in Fig. 40(d-f). In the present case, they are computed from the deformation gradient, which is constant along an element. Thus the "pixelization" of the strain maps is due to the underlying mesh used in the RT3-DIC calculations. The central part of the pantographic structure contracts more in the transverse direction (ϵ_{xx}) than its longitudinal expansion (ϵ_{yy}). This phenomenon is accompanied with more moderate shear (ϵ_{xy}).

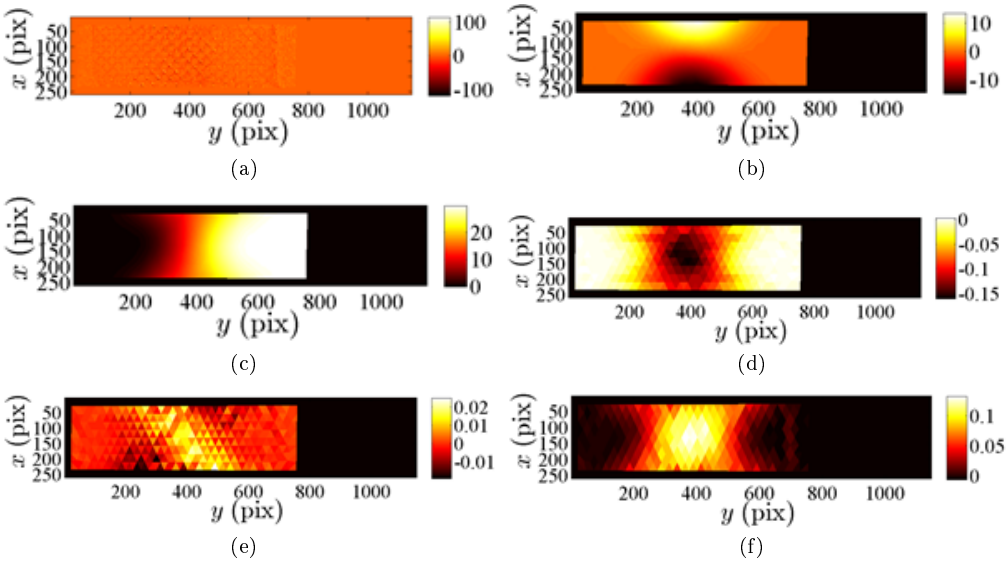

Fig. 40 Correlation results for the 5th loading step: (a) gray level residuals, (b) u_x and (c) u_y displacement fields (expressed in pixels). (d) ϵ_{xx}, (e) ϵ_{yy} (f) ϵ_{xy} nominal strain fields.

In Fig. 41 the same fields are shown. The gray level residuals only slightly degrade in comparison with the previous loading step (Fig. 41(a)). The pattern of the transverse and longitudinal displacement fields is very similar with higher overall levels. The same observation applies for the strain fields. The deformation mode remains unchanged. It is worth observing that all strain levels in the grips remain close to zero, which is to be expected. This is a further validation of the present results.

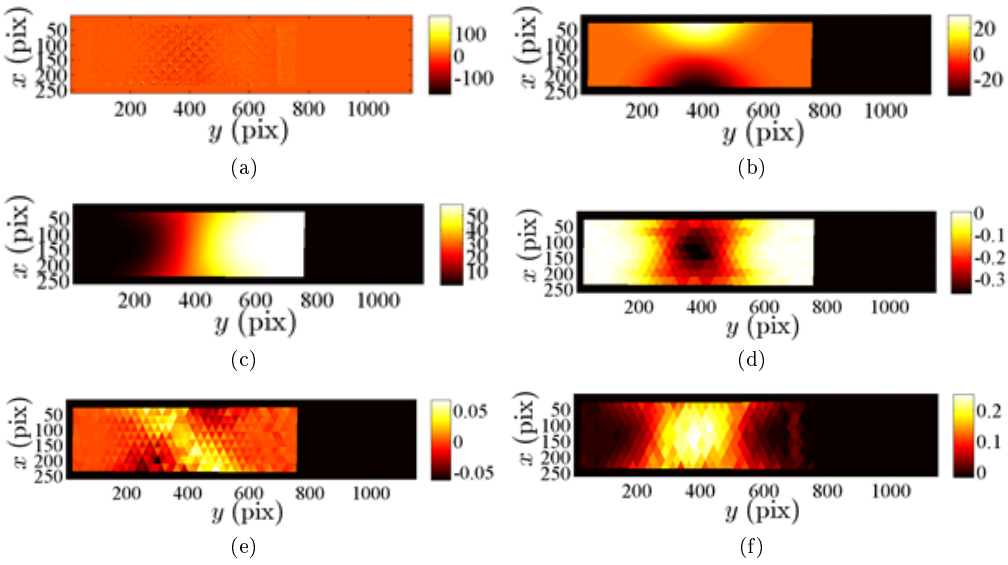

Fig. 41 Correlation results for the 10th loading step: (a) gray level residuals, (b) u_x and (c) u_y displacement fields (expressed in pixels). (d) ϵ_{xx}, (e) ϵ_{yy} (f) ϵ_{xy} nominal strain fields.

The last load level prior to damage inception (i.e. first strut failure) is reported in Figure e. In that case the gray level residuals (Fig. 42 (a)) are significantly higher than the previous two cases (Figs. 40(a) and 41(a)). The chosen kinematics is no longer able to properly describe, in a continuous way, the actual kinematics of the central region of the pantographic structure. For the parts of the pantographic sheet closer to the grips and the grips themselves, the registration quality is significantly better. This result validates the choice of including part of the speckled grips in the analysis. For this last step, the highly deformed region has grown toward both ends of the pantographic sheet, which can be understood by the fact that when struts touch each other, the deformation mechanism moves away from these zones.

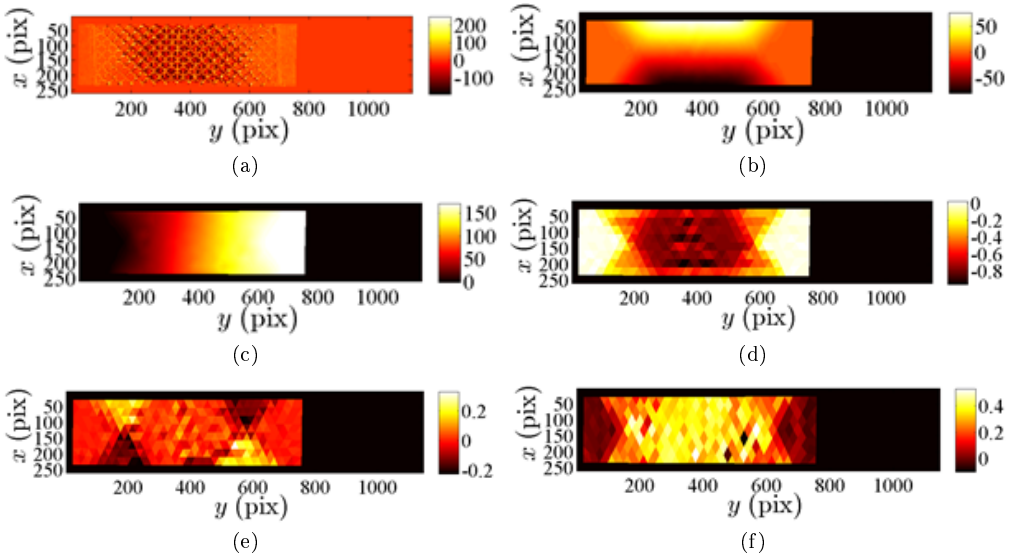

Fig. 42 Correlation results for the 30th loading step: (a) gray level residuals, (b) u_x and (c) u_y displacement fields (expressed in pixels). (d) ϵ_{xx}, (e) ϵ_{yy} (f) ϵ_{xy} nominal strain fields.

The DIC results reported herein show that such analyses can be run on pantographic structures. Prior to damage inception, longitudinal nominal strains of the order of 50% and transverse strains as high as 90% were achieved. Such levels could be measured thanks to the sample preparation followed herein. Namely, the grips of the pantographic sheet were speckled. In the future, it is likely that speckled pantographic structures should be analyzed in order to make the DIC analyses easier. It was also shown that a continuous displacement basis was only partly capturing the actual kinematics of the experiment. This calls for more advanced registration techniques that would be consistent with the particular geometry of the pantographic structures and their specific kinematics.

4 Conclusion and outlook

Pantographic fabrics proved to be a very interesting subject of study, involving the work of, at least, (Computational) Mechanicians (modelling), Experimentalists (experiments), Numerical Analysts (model solving), Data Analysts (image correlation), Mathematicians (well-posedness and Γ-convergence) and many other researchers and professionals. We believe that what has been presented in this survey can thus be considered our manifesto about how commitment from different groups of researchers should be directed for the study of metamaterials and, more generally, for the

study of every scientific subject. Mechanics, as any other natural Science, cannot proceed without a continuous interplay between experimental evidence and theoretical modelling.

However, this is just a first simple step toward the study of more complex structures and experiments. A famous quote by Hilbert states that "*the art of doing mathematics consists in finding that special case which contains all the germs of generality.*" This statement can be extended to every scientific discipline, including those that have been applied in the studies presented in this survey, and that pantographic fabrics can be considered as one of the simplest example leading to treat non-standard problems in mechanics of materials and its related disciplines. In this sense, pantographic structures provide the minimal setting for the study of relevant issues in Mechanics. The solution of a general problem is easier to face once that of its particular cases has been addressed, as, very often, particular cases help to understand better the real nature of the problem. Currently, new tests and structures are being studied, along with their technological realization challenges, like the three-point test shown in Fig. 43(a) and the pantographic sheet with "perfect" pivots, i.e. hinges that do not oppose to variations of the shear angle between two intersecting fibers, shown in Fig. 43(b).

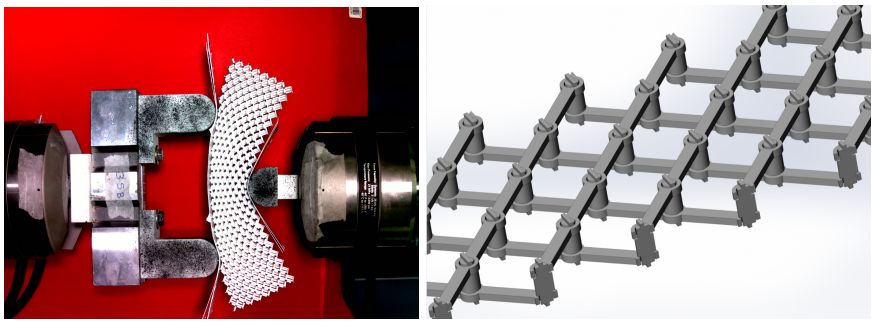

(a) (b)

Fig. 43 (a) Three-point flexural test on a 3D pantographic specimen. (b) Pantographic sheet with "perfect" hinges.

References

1. F. dell'Isola, D. Steigmann, and A. Della Corte. Synthesis of fibrous complex structures: Designing microstructure to deliver targeted macroscale response. *Applied Mechanics Reviews*, 67(6):060804, 2015.
2. Graeme Milton, Marc Briane, and Davit Harutyunyan. On the possible effective elasticity tensors of 2-dimensional and 3-dimensional printed materials. *Mathematics and Mechanics of Complex Systems*, 5(1):41–94, 2017.
3. Victor A Eremeyev and Wojciech Pietraszkiewicz. Material symmetry group and constitutive equations of micropolar anisotropic elastic solids. *Mathematics and Mechanics of Solids*, 21(2):210–221, 2016.
4. Albrecht Bertram and Rainer Glüge. Gradient materials with internal constraints. *Mathematics and Mechanics of Complex Systems*, 4(1):1–15, 2016.
5. Lucio Russo. *The forgotten revolution: how science was born in 300 BC and why it had to be reborn*. Springer Science & Business Media, 2013.
6. Stephen M Stigler. Stigler's law of eponymy. *Transactions of the New York Academy of Sciences*, 39(1 Series II):147–157, 1980.
7. F. dell'Isola, U. Andreaus, and L. Placidi. At the origins and in the vanguard of peridynamics, non-local and higher-gradient continuum mechanics: An underestimated and still topical contribution of Gabrio Piola. *Mathematics and Mechanics of Solids*, 20(8):887–928, 2015.
8. F. dell'Isola, A. Della Corte, and I. Giorgio. Higher-gradient continua: The legacy of Piola, Mindlin, Sedov and Toupin and some future research perspectives. *Mathematics and Mechanics of Solids*, 22(4):852–872, 2017.
9. D. Del Vescovo and I. Giorgio. Dynamic problems for metamaterials: review of existing models and ideas for further research. *International Journal of Engineering Science*, 80:153–172, 2014.
10. F. dell'Isola, T. Lekszycki, M. Pawlikowski, R. Grygoruk, and L. Greco. Designing a light fabric metamaterial being highly macroscopically tough under directional extension: first experimental evidence. *Zeitschrift für angewandte Mathematik und Physik*, 66:3473–3498, 2015.
11. J-J. Alibert, P. Seppecher, and F. dell'Isola. Truss modular beams with deformation energy depending on higher displacement gradients. *Mathematics and Mechanics of Solids*, 8(1):51–73, 2003.
12. Catherine Pideri and Pierre Seppecher. A second gradient material resulting from the homogenization of an heterogeneous linear elastic medium. *Continuum Mechanics and Thermodynamics*, 9(5):241–257, 1997.
13. F. dell'Isola, I. Giorgio, M. Pawlikowski, and N. Rizzi. Large deformations of planar extensible beams and pantographic lattices: heuristic homogenization, experimental and numerical examples of equilibrium. *Proc. R. Soc. A*, 472(2185):23 pages, 2016.
14. F. dell Isola, P. Seppecher, and A. Della Corte. The postulations á la d alembert and á la cauchy for higher gradient continuum theories are equivalent: a review of existing results. In *Proc. R. Soc. A*, volume 471, page 20150415. The Royal Society, 2015.
15. N. Auffray, F. dell'Isola, V. Eremeyev, A. Madeo, and G. Rosi. Analytical continuum mechanics à la Hamilton–Piola least action principle for second gradient continua and capillary fluids. *Mathematics and Mechanics of Solids*, 20(4):375–417, 2015.
16. H. Altenbach and V. Eremeyev. On the linear theory of micropolar plates. *ZAMM-Journal of Applied Mathematics and Mechanics/Zeitschrift für Angewandte Mathematik und Mechanik*, 89(4):242–256, 2009.
17. W. Pietraszkiewicz and V. Eremeyev. On natural strain measures of the non-linear micropolar continuum. *International Journal of Solids and Structures*, 46(3):774–787, 2009.
18. Y. Rahali, I. Giorgio, J.F. Ganghoffer, and F. dell'Isola. Homogenization à la piola produces second gradient continuum models for linear pantographic lattices. *International Journal of Engineering Science*, 97:148–172, 2015.
19. A. Bilotta, G. Formica, and E. Turco. Performance of a high-continuity finite element in three-dimensional elasticity. *International Journal for Numerical Methods in Biomedical Engineering*, 26(9):1155–1175, 2010.
20. A. Cazzani, M. Malagù, and E. Turco. Isogeometric analysis: a powerful numerical tool for the elastic analysis of historical masonry arches. *Continuum Mechanics and Thermodynamics*, 28(1-2):139–156, 2016.
21. M de Saint-Venant. *Mémoire sur la torsion des prismes: avec des considérations sur leur flexion ainsi que sur l'équilibre intérieur des solides élastiques en général: et des formules pratiques pour le calcul de leur résistance à divers efforts s' exerçant simultanément*. Imprimerie nationale, 1856.
22. RD Mindlin and HF Tiersten. Effects of couple-stresses in linear elasticity. *Archive for Rational Mechanics and analysis*, 11(1):415–448, 1962.
23. OW Dillon and P Perzyna. Gradient theory of materials with memory and internal changes. *ARCHIVES OF MECHANICS*, 24(5-6):727–747, 1972.
24. H Abdoul-Anziz and Pierre Seppecher. Strain gradient and generalized continua obtained by homogenizing frame lattices. 2017.
25. Emilio Turco, Ivan Giorgio, Anil Misra, and Francesco dell'Isola. King post truss as a motif for internal structure of (meta) material with controlled elastic properties. *Open Science*, 4(10):171153, 2017.
26. G.C. Everstine and A.C. Pipkin. Boundary layers in fiber-reinforced materials. *J. Appl. Mech.*, 40:518–522, 1973.

27. M.G. Hilgers and A.C. Pipkin. Elastic sheets with bending stiffness. *Q. J. Mech. Appl. Math.*, 45:57–75, 1992.
28. M.G. Hilgers and A.C. Pipkin. Energy-minimizing deformations of elastic sheets with bending stiffness. *J. Elast.*, 31:125–139, 1993.
29. M.G. Hilgers and A.C. Pipkin. Bending energy of highly elastic membranes ii. *Q. Appl. Math*, 54:307–316, 1996.
30. M.Z. Hu, H. Kolsky, and A.C. Pipkin. Bending theory for fiber-reinforced beams. *J. Compos. Mater*, pages 235–249, 1985.
31. A.C. Pipkin. Generalized plane deformations of ideal fiber-reinforced materials. *Q. Appl. Math*, 32:253–263, 1974.
32. A.C. Pipkin. Energy changes in ideal fiber-reinforced composites. *Q. Appl. Math*, 35:455–463, 1978.
33. A.C. Pipkin. Some developments in the theory of inextensible networks. *Q. Appl. Math*, 38:343–355, 1980.
34. F. dell'Isola, M.V. d'Agostino, A. Madeo, P. Boisse, and D. Steigmann. Minimization of shear energy in two dimensional continua with two orthogonal families of inextensible fibers: the case of standard bias extension test. *Journal of Elasticity*, 122(2):131–155, 2016.
35. L. Placidi, L. Greco, S. Bucci, E. Turco, and N.L. Rizzi. A second gradient formulation for a 2d fabric sheet with inextensible fibres. *Zeitschrift für angewandte Mathematik und Physik*, 67(5)(114), 2016.
36. RS Rivlin. Plane strain of a net formed by inextensible cords. In *Collected Papers of RS Rivlin*, pages 511–534. Springer, 1997.
37. I. Giorgio. Numerical identification procedure between a micro-cauchy model and a macro-second gradient model for planar pantographic structures. *Zeitschrift für angewandte Mathematik und Physik*, 67(4)(95), 2016.
38. E. Turco, F. dell'Isola, A. Cazzani, and N.L. Rizzi. Hencky-type discrete model for pantographic structures: numerical comparison with second gradient continuum models. *Zeitschrift für angewandte Mathematik und Physik*, 67:28 pages, 2016.
39. Victor A Eremeyev, Francesco dell'Isola, Claude Boutin, and David Steigmann. Linear pantographic sheets: existence and uniqueness of weak solutions. 2017.
40. L. Placidi, E. Barchiesi, E. Turco, and N.L. Rizzi. A review on 2D models for the description of pantographic fabrics. *Zeitschrift für angewandte Mathematik und Physik*, 67(5)(121), 2016.
41. F. dell'Isola and D.J. Steigmann. A two-dimensional gradient-elasticity theory for woven fabrics. *J. Elasticity*, 18:113–125, 2015.
42. I. Giorgio, R. Grygoruk, F. dell'Isola, and D.J. Steigmann. Pattern formation in the three-dimensional deformations of fibered sheets. *Mechanics Research Communications*, 69:164–171, 2015.
43. I. Giorgio, N.L. Rizzi, and E. Turco. Continuum modelling of pantographic sheets for out-of-plane bifurcation and vibrational analysis. *Proc. R. Soc. A*, page 21 pages, 2017 (http://dx.doi.org/10.1098/rspa.2017.0636).
44. N. Auffray, J. Dirrenberger, and G. Rosi. A complete description of bi-dimensional anisotropic strain-gradient elasticity. *International Journal of Solids and Structures*, 69:195–206, 2015.
45. C. Boutin, F. dell'Isola, I. Giorgio, and L. Placidi. Linear pantographic sheets: Asymptotic micro-macro models identification. *Mathematics and Mechanics of Complex Systems*, 5(2):127–162, 2017.
46. L. Placidi, U. Andreaus, A. Della Corte, and T. Lekszycki. Gedanken experiments for the determination of two-dimensional linear second gradient elasticity coefficients. *Zeitschrift für angewandte Mathematik und Physik*, 66(6):3699–3725, 2015.
47. L. Placidi, E. Barchiesi, and A. Battista. An inverse method to get further analytical solutions for a class of metamaterials aimed to validate numerical integrations. In *Mathematical Modelling in Solid Mechanics*, pages 193–210. Springer, 2017.
48. D. Scerrato, I.A. Zhurba Eremeeva, T. Lekszycki, and N.L. Rizzi. On the effect of shear stiffness on the plane deformation of linear second gradient pantographic sheets. *ZAMM-Journal of Applied Mathematics and Mechanics/Zeitschrift für Angewandte Mathematik und Mechanik*, 96(11):1268–1279, 2016.
49. F. dell'Isola, I. Giorgio, and U. Andreaus. Elastic pantographic 2d lattices: a numerical analysis on static response and wave propagation. In *Proceedings of the Estonian Academy of Sciences*, volume 64, pages 219–225, 2015.
50. F. dell'Isola, A. Della Corte, I. Giorgio, and D. Scerrato. Pantographic 2D sheets: Discussion of some numerical investigations and potential applications. *International Journal of Non-Linear Mechanics*, 80:200–208, 2016.
51. A. Madeo, A. Della Corte, L. Greco, and P. Neff. Wave propagation in pantographic 2d lattices with internal discontinuities. *arXiv preprint arXiv:1412.3926*, 2014.
52. E. Turco, F. dell'Isola, N.L. Rizzi, R. Grygoruk, W.H. Müller, and C. Liebold. Fiber rupture in sheared planar pantographic sheets: Numerical and experimental evidence. *Mechanics Research Communications*, 76:86–90, 2016.
53. M. Spagnuolo, K. Barcz, A. Pfaff, F. dell'Isola, and P. Franciosi. Qualitative pivot damage analysis in aluminum printed pantographic sheets: numerics and experiments. *Mechanics Research Communications*, 2017.
54. G. Ganzosch, F. dell'Isola, e. Turco, T. Lekszycki, and W.H. Müller. Shearing tests applied to pantographic structures. *Acta Polytechnica CTU Proceedings*, 7:1–6, 2016.

55. E. Turco, M. Golaszewski, I. Giorgio, and F. D'Annibale. Pantographic lattices with non-orthogonal fibres: Experiments and their numerical simulations. *Composites Part B: Engineering*, 118:1–14, 2017.
56. Michael A Sutton, Jean Jose Orteu, and Hubert Schreier. *Image correlation for shape, motion and deformation measurements: basic concepts, theory and applications*. Springer Science & Business Media, 2009.
57. Francois Hild and Stéphane Roux. *Digital image correlation*. Wiley-VCH, Weinheim, 2012.
58. Zvonimir Tomičević, François Hild, and Stéphane Roux. Mechanics-aided digital image correlation. *The Journal of Strain Analysis for Engineering Design*, 48(5):330–343, 2013.
59. Hugo Leclerc, Jean-Noël Périé, Stéphane Roux, and François Hild. Integrated digital image correlation for the identification of mechanical properties. In *International Conference on Computer Vision/Computer Graphics Collaboration Techniques and Applications*, pages 161–171. Springer, 2009.
60. François Hild, Stéphane Roux, Renaud Gras, Néstor Guerrero, Maria Eugenia Marante, and Julio Flórez-López. Displacement measurement technique for beam kinematics. *Optics and Lasers in Engineering*, 47(3):495–503, 2009.
61. François Hild and Stéphane Roux. Comparison of local and global approaches to digital image correlation. *Experimental Mechanics*, 52(9):1503–1519, 2012.